CHALMERS

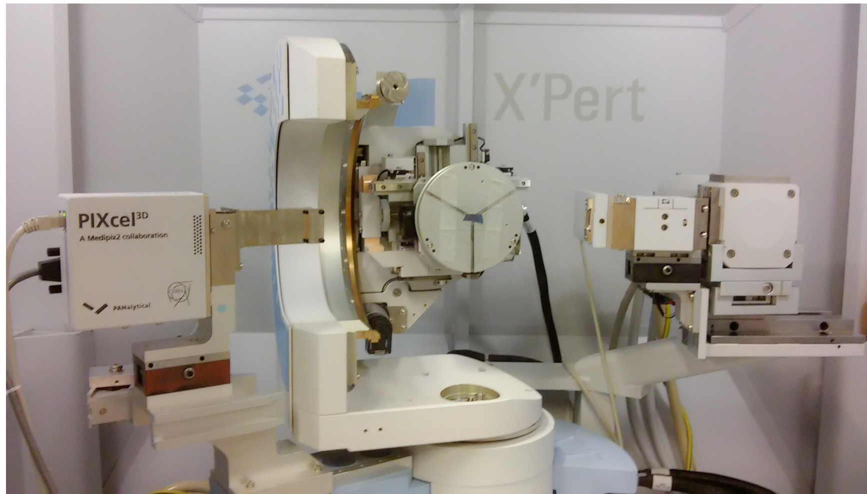

HRXRD Characterization of MBE Epitaxial Materials and Related Nanostructures

Thesis for Erasmus Mundus Master of Science in Nanoscience and Nanotechnology

FITRIA RAHAYU

Department of Microtechnology and Nanoscience
Terahertz and Millimetre Wave Laboratory
CHALMERS UNIVERSITY OF TECHNOLOGY
Gothenburg, Sweden 2015

Education and Culture
Erasmus Mundus

KATHOLIEKE UNIVERSITEIT
LEUVEN

Thesis for Master Degree

HRXRD Characterization of MBE Epitaxial Materials and Related Nanostructures

FITRIA RAHAYU

Supervisor: Huan Zhao, Chalmers
Co-promoter: Prof. Wilfried Vandervorst, KU Leuven
Referee: Thilo Bauch, Chalmers

Department of Microtechnology and Nanoscience - MC2
Terahertz and Millimetre Wave Laboratory
Chalmers University of Technology
Gothenburg, Sweden 2015

HRXRD Characterization of MBE Epitaxial Materials and Related Nanostructures
FITRIA RAHAYU

© Fitria Rahayu, 2015.

Master's Thesis 2015
Department of Microtechnology and Nanoscience - MC2
Terahertz and Millimetre Wave Laboratory
Chalmers University of Technology
SE-412 96 Gothenburg
Telephone +46 31 772 1000

Cover: HRXRD PANalytical X'pert Pro of MC2 Chalmers clean room.

This report is written in LaTeX
Printed by Chalmers
Gothenburg, Sweden 2015

Abstract

For high performance semiconductor electronics and optoelectronics, the quality of the materials used for device fabrication is critical to the device performance. Therefore, material characterization is an essential step in a device fabrication process. X-ray diffraction (XRD) is a powerful nondestructive technique for characterizing crystalline materials, e.g semiconductor materials. It provides information on structures, phases, preferred crystal orientations, and other structural parameters, such as average grain size, crystallinity, strain, and crystal defects.

The aim of this thesis is to explore different configurations of the XRD system and measurement methods on different materials, and to understand better that for different materials which techniques provide the fastest and simplest approach to acquire the results. Different semiconductor materials including InAs & InGaAs thin films, and InAs nanowires were characterized in this project. All the materials were grown by molecular beam epitaxy (MBE).

The InAs and InGaAs thin films were grown on GaAs substrate, with the layer partially or fully relaxed. High resolution XRD (HRXRD) measurements were carried out on these samples. Two methods, based on rocking curve (RC) scans and reciprocal space mapping (RSM), respectively, were used to calibrate In composition and to characterize strain relaxation. The two methods show consistent results, implying the accuracies. Considering the simplicity of the two methods, it is much easier and faster to get the tilt using the rocking curve method, whereas the RSM method requires less effort on measurement set up and calculation. However, the RSM method takes much longer scanning time compared to the RC method.

The InAs nanowires were grown on Si (111) substrate. This is because nanowires with cubic crystal typically grow in the (111) direction and therefore they are often epitaxial grown on (111) substrate to achieve vertical aligned nanowire growth. However, it is widely observed that the crystallographic structure of GaAs, InAs, and some other III-V nanowires embody occasional staking faults (SFs) originating from the presence of mixed wurtzite (WZ) and zincblend (ZB) structures. Transmission Electron Microscopy (TEM) has been a powerful tool to characterize the crystalline phase in atomic scale, however, it usually require complex sample preparation and extremely high image resolution. In this work, different XRD configurations have

been used to characterize the InAs nanowire crystalline structures. RC scans seems invalid to provide full information since the diffraction peaks from the WB and ZB structures appears at different offsets. RSM measurements were carried out under both HRXRD and x-ray lens configurations, showing similar results. TEM measurements were carried out to verify the XRD results.

Keywords: X-ray diffraction, HRXRD, X-ray Lens, Semiconductor, Nanowires.

Acknowledgements

First of all, I would like to thank Allah S.W.T for His blessings and for giving me health and strength to finish this project. May His blessings and peace be upon the messenger of Allah, Muhammad S.A.W, his family and companions.

I would like to express my heartiest gratitude and appreciation to my supervisor, Huan Zhao, for the opportunity to work on this project and for her guidance, persistent help, valuable suggestions, and all support during the work of this project. I would also like to thank all members of Terahertz and Millimetre Wave Laboratory, especially to Alexandra and Elham, for all kindness and cooperation during my stay in this group.

I owe a deep sense of gratitude to Alexei Kalaboukhov for the great help with the equipments, and also to Anton Davydok from IM2NP, France for the fruitful discussion even though we have never actually met.

I wish to thank profusely Prof. Wilfried Vandervorst for his willingness to evaluate my thesis. I also want to express my gratitude to the European commission for giving me the financial support and the opportunity to study in this master program. I humbly extends my gratitude to Prof. Guido Groeseneken, Ms. Elke Delfosse, and all members in EMM-Nano programme for the guidance and support. Special thanks to all my friends in EMM-Nano programme, this programme was enjoyable largely because of you guys.

Last but not least, I am hugely indebted to my beloved parents, brothers, and sisters for all moral support and untiring love. I would also like to express my special biggest gratitude to my dearest husband for always being there for me and for all the encouragement, help, and the numerous midnight cups of sweet tea during these past two years.

Fitria Rahayu
Gothenburg
August 19, 2015

Contents

List of Figures **xiv**

List of Tables **xviii**

1 Introduction **1**

2 Principle of X-Ray Diffraction **5**

2.1 Bragg's Law 5

2.2 Reciprocal Space 6

2.2.1 Laue condition and Ewald's sphere 8

3 Semiconductor Materials and Molecular Beam Epitaxy **11**

3.1 Semiconductor Material 11

3.1.1 Lattice constant 13

3.2 Semiconductor heterostructures 15

3.2.1 Chemical composition 15

3.2.2 Lattice mismatch, strain, and relaxation 16

3.3 Molecular beam epitaxy 17

4 XRD measurement **19**

4.1 Instrumentation 19

4.1.1 X-ray beam source 19

4.1.2 Incident optics 20

4.1.3 Sample stage 22

4.1.4 Diffracted beam optics 22

4.2 Instrument configurations, measurement methods, and scan types . . 25

4.2.1 Configuration types 25

4.2.1.1 HRXRD 25

4.2.1.2 X-ray Lens 25

4.2.2 Measurement types 26

4.2.2.1 Diffraction planes 26

4.2.2.2 Out of Plane Measurement 27

4.2.2.3 In Plane Measurement 28

4.2.2.4 X-Ray Reflectivity Measurement 29

4.2.3 Scan types 30

4.2.3.1 Rocking curve 30

4.2.3.2 Reciprocal Space Mapping (RSM) 32

4.3 Summary 35

5 XRD Measurements on Thin Film Samples **37**

5.1 InAs film on GaAs substrate 37

5.1.1 Measurements and results 38

5.1.2 Calculation method 40

5.1.2.1 Calculation from RC result 40

5.1.2.2 Calculation from RSM result 42

5.1.3 Discussion 44

5.2 $In_xGa_{1-x}As$ layers on GaAs substrate 45

5.2.1 Measurement and Results 45

5.2.2 Calculation method 47

5.2.2.1 Calculation from RC result 49

5.2.2.2 Calculation from RSM result 50

5.2.3 Discussion 51

6 XRD Measurements on Nanowire Samples 53

6.1 Nanowire structure 53

6.2 Nanowire grow with MBE 55

6.3 Nanowire Characterization 57

6.3.1 HRXRD configuration 58

6.3.2 X-ray lens configuration 61

6.3.2.1 Out of plane X-ray lens measurement 61

6.3.2.2 In plane X-ray lensmeasurement 63

6.4 Transmission electron microscopy (TEM) 66

6.5 Discussion 69

7 Conclusion 73

References **75**

A Appendix A : Bragg angles **I**

B Appendix B : Out of Plane Sample Alignment **III**

B.1 Reciprocal Space Mapping Procedure IV

C Appendix C : Time Comparison **V**

List of Figures

2.1 Schematic drawing illustrate Bragg condition of diffraction. Constructive interference occurs when the path difference between two rays equal to 2dsinθ 6

2.2 Construction of Ewald's sphere satisfying K=k-k' 9

2.3 A reciprocal lattice observed within an Ewald's sphere. Red spots represents the planes of atoms in a crystal 9

3.1 Energy bands of conductor, semiconductor and insulator 12

3.2 (a) diamond crystal structure and (b) zinc blende crystal structure . . 12

3.3 (a) hexagonal crystal structure and (b) wurtzite crystal structure . . 13

3.4 Band gap and lattice constant for various III-V and group IV material alloy 14

3.5 Strain and relaxation in lattice mismatched epitaxial layer on substrate. Figure on the right shows how a relaxation of strain can cause a defect in a grown layer 17

3.6 Riber Compact C21 MBE system used in this work [1] 17

4.1 Hybrid monochromator used in most measurement in this work . . . 20

4.2 (a) schematic of X-ray lens and (b) total reflection inside glass capillary 21

4.3 X-ray lens incident beam optic used in this work 21

4.4 Schematic of sample stage movements 22

4.5 Pixcel 3D detector 23

4.6 Static line mode (115) 2theta measurements of an InAs sample for different amount of measurement time 24

4.7 Parallel plate collimator used in X-ray lens configuration 24

4.8 High resolution XRD diffractometer configuration 25

4.9 X-ray lens configuration 26

4.10 Geometry for (a)symmetrical and (b)asymmetrical out of plane diffraction 26

4.11 Examples of symmetric and asymmetric crystal planes 27

4.12 Out of plane XRD configuration 27

4.13 In plane XRD measurement set up 28

4.14 Illustration of perpendicular lattice planes in cubic and hexagonal lattice 29

4.15 XRR results giving information about thickness and surface roughness 30

4.16 Out-of-plane rocking curve measurements of an InAs film grown on GaAs substrate (a) (004) omega scan, (b) (004) omega-2theta scan, (c) (115) 2theta scan, and (d) (115) 2theta-omega scan 31

4.17 RSM example on different intensity scales 33

4.18 (a)RSM in angular coordinates mode, (b)RSM projection into x-axis, and (c)Projected x-axis combined with omega-2theta coupled scan result 34

4.19 Schematic drawing explains RSM data analysis for (a)tilt seen from a symmetric scan, (b)fully relaxed layer, and (c)fully strained layer . 34

5.1 Symmetrical and asymmetrical RC peak shift between $\phi = 0^o$ and $\phi = 1800^o$ due to tilt. Tilt will cause a change in peak splitting $\delta\omega$ between substrate and epilayer when it is seen from different azimuths 38

5.2 RSM (004) of InAs on GaAs at (a)$\phi = 0^o$ and (b)$\phi = 180^o$ 39

5.3 Summary of RSM scans of both (004) and (115) in one RSM graph . 39

5.4 Parameters that changes due to strain in lattices at $\phi = 0^o$ and $\phi = 180^o$ 41

5.5 d-spacing calculation with relative measurement approach 43

5.6 Coupled scan result of (004) and (115) plane of $In_xGa_{1-x}As$ on GaAs for $\phi = 0^o$ and $\phi = 180^o$ 46

5.7 RSM(004) for $\phi = 0^o$ and $\phi = 180^o$ of $In_xGa_{1-x}As$ on GaAs 47

5.8 Combined graph of RSM(004) and RSM(115) of $In_xGa_{1-x}As$ on GaAs 47

5.9 RSM (115) of $In_xGa_{1-x}As$ layers on GaAs. Second layer is more strained than the other layers. 52

6.1 Nanowire atom structure in zinc blende and wurtzite phases grown in $<111>_c$ or $<0001>_h$ direction 54

6.2 Types of stacking faults: (a) intrinsic (missing an A plane), (b) extrinsic (extra B plane) and (c) twinning (A plane as twin boundary) . 55

6.3 Sample A, B, and C as seen using SEM. Left figures are the side view (75° tilt) and right figures are the top view (except samples C is 30° tilt). Top view shows hexagonal geometry of grown nanowires. 57

6.4 (331) coupled scan of sample A, B, and C 59

6.5 a) and (c) RSM scan results of sample A and C show (105)WZ, (422)ZB, and (331)ZB peaks at the same Qx. (b) RSM scan result of sample B indicates a presence of wurtzite rich phase nanowires 60

6.6 (a) Sample B RSM with substrate peak. Peak intensity is dominated by substrate's peak. (b) Nanowire peak is presented clearly after carefully aligning 61

6.7 (a), (b), and (c) Coupled scan results for sample A, B, and C using X-ray lens measurement respectively. (d) shows coupled scan result from the substrate. The peaks are totally dominated by substrate's peaks 62

6.8 (a), (b), and (c) RSM scan results using X-ray lens measurement. (422)ZB, (105)WZ, and (331)ZB peaks appear in the graph for sample A and C, while only (105)WZ appears in the graph for sample B. . . 64

6.9 In plane measurement result on sample B 65

6.10 TEM results and calculated diffraction spots for sample A and B. Left pictures are the actual TEM images, right pictures are the zoom in of the images, and bottom images are the FFT results of the images. 68

6.11 TEM images observation showing defect free, rotational twins, and intrinsic and extrinsic stacking faults in InAs and $InAs_{1-x}Sb_x$ nanowires 69

List of Tables

3.1 Bulk lattice constant of common known materials 14

4.1 Comparison on Receiving slit and Scanning line 23

4.2 FWHM comparisons of X-ray lens and HRXRD RSM results 35

5.1 Data from RC scan $\omega - 2\theta$ scan 38

5.2 Data from RSM scans of InAs on GaAs sample 40

5.3 InAs on GaAs RC calculation results 42

5.4 InAs on GaAs RSM calculation results 44

5.5 Data of $In_xGa_{1-x}As$ on GaAs sample from RC scan result 46

5.6 Data of $In_xGa_{1-x}As$ on GaAs sample from RSM scan result 48

5.7 In composition, Poisson's ratio and relaxed d spacing results from iterative calculation 49

5.8 RC calculation results of $In_xGa_{1-x}As$ on GaAs sample 50

5.9 Tilt calculation results from RSM 50

5.10 RSM calculation results of $In_xGa_{1-x}As$ on GaAs sample 50

6.1 Nanowire samples data 56

6.2 FWHM comparisons of X-ray lens and HRXRD RSM results 65

6.3 (Top) Calculation results adapted from [2], and (bottom) calculation results based on TEM results for sample A and B 67

6.4 Lattice parameter in zinc blende and wurtzite calculation for sample A, B and C 71

A.1 Bragg and tilt angles of common substrates I

C.1 Measurement time comparison table for each configuration and scan type V

1

Introduction

X-ray diffraction (XRD) is one commonly used technique to characterize material's structural properties. XRD technique has been widely used for decades in order to find the structural properties of many types of material, such as polymers[3], dielectrics, powder, crystal, etc. XRD measurements can provide many useful information such as structural composition, thickness, mismatch, relaxation, dislocation density, mosaic spread, curvature, and surface damage. XRD has several advantages compared to other characterization technique, including; non-destructive, non-complicated preparation, and can be used in ambient atmosphere. In this work, we mainly discuss the application of XRD on characterization of III-V compound semiconductors.

Nowadays a significant volume of semiconductor devices and circuits employs III–V compound technology. Compared with silicon, which have been dominating the semiconductor industry for more than half century, III-V compound semiconductors feature a direct band gap and a much higher electron mobility, showing more attractive applications in light emitting and high speed electronics. And with compound semiconductors, heterostructures can be formed by integration of dissimilar materials, which enables engineering the electronic energy bands for a better device design. And in a heterostructure, materials and their combination can be tailor made in nano-scale showing unique quantum effects, which is unattainable in their bulk constituents, thanks to the sophisticated epitaxial growth method such as molecular beam epitaxy (MBE). Based on these, uncounted numbers of compound semiconductor devices with a wide variety of functions have been developed.

For epitaxy of compound heterostructures, careful control of the composition is important. XRD is the most commonly used methods to calibrate com-

positions and extract the growth rate, which is very important to epitaxy growth. Another important issue has to be addressed for epitaxy is the lattice mismatch. Heterostructures are not formed without any limitation. One of the biggest technological challenges is that a device quality heterostructure has to be grown with its lattice constant equal or close to that of a substrate to avoid deleterious structural defects. However, the types of available substrates are limited to a few numbers. Therefore lattice mismatched epitaxy is vital to synthesizing a wide range of materials to realize devices for any desired application, and various epitaxy techniques have been developed such as metamorphic growth methods, patterned substrate growth, compliant substrate and etc [3] . All these approaches tried to block the dislocations nearby the interface between the substrate and epilayer, to obtain a strain-free layer with same or similar lattice constant to the device epi-structures. In this case, XRD is usually used to study the residue strain and compositions of epilayers. In this work, as an example, XRD is used to characterize the strain and/or composition of InAs and InGaAs thin films, which are grown lattice mismatched on GaAs substrates.

Driven by the great benefits brought by monolithic integration of III-V and Si, epitaxy of III-V 1dimensional (1D) materials, i.e. nanowires on Si has attract more and more attention. This is because the 1D structure can accommodate a greater elastic strain with respect to the host substrate than is commonly seen with planar interfaces, because the free borders at the side walls allow for lateral strain relaxation [4].

Growth of III-V nanowires on Si(111) exhibit vertical directionality in (111) direction with hexagon shaped geometries. The layer by layer growing mechanism of nanowires makes it possible for two phases to form, i.e. zinc blende or wurtzite. It is also possible for the structure to be a mix of both phases. The different phases of nanowires exhibit different lattice constant, and hence also energy gap. In this thesis, the characterization of nanowire samples will be mainly focused to find the phase of InAs nanowires grown on top of Si(111). Compared to Transmission Electron Microscopy which also provides structural information of a material that is destructive, more expensive, and only characterize single NW, XRD provides non destructive, cheaper, and allows characterization of an ensamble of nanowires. Results of XRD of these samples will be supported using TEM and SEM.

The main aim of this thesis is to get familiar with the techniques of using

the XRD equipment and apply this techniques in researches conducted at Terahertz Milimetre Laboratory group. In this thesis, characterizations of different types of materials, including InAs thin film, compositionally graded $In_xGa_{1-x}As$, and InAs nanowires samples will be explained. The outline of this thesis is as follows:

- Chapter 2 describes the fundamental theories on X-Ray diffraction.
- Chapter 3 explains some theories on crystallography and MBE growth.
- Chapter 4 presents the equipment used in this work, the different optic configuration, measurement methods, and scan types that can be used with the equipment.
- Chapter 5 will explain the methodologies used to extract the material properties from the scans and discuss the results for InAs thin film and compositionally graded $In_xGa_{1-x}As$ samples.
- Chapter 6 will discuss thoroughly about nanowire from the fundamental theories, XRD measurement methods, results and discussion.
- Chapter 7 summarizes the main conclusions of this work.

2

Principle of X-Ray Diffraction

The interactions between an electromagnetic (EM) field and a solid in solid state physics includes diffraction, absorption, scattering, transmission, and reflection. In this chapter, the interaction of an EM field with crystal will be discussed.

2.1 Bragg's Law

When an EM field encounters a hole or a slit, a diffraction pattern appears. In the case of a light beam, a pattern of bright and dark pattern as a result a breakup of the light beam could be seen. Some of the light beams interfere constructively with each other and create bright area while others interfere destructively with each other and turns into dark areas. A constructive interference can be achieved when the path difference of two light beams, that is the difference of the distances the two light beams travelling from the slit to the screen, is a multiplication of the wavelength, i.e $n\lambda$ where n is an integer.

In solid state physics, diffraction occurs as a result of the interactions between EM radiaton and atoms in a crystal which result in a constructive interference[5]. The spacing between the planes of atoms are regarded in the same way as the slits in the general diffraction description. To be able to get a diffraction pattern of a crystal, an EM radiation with wavelength comparable to the atoms is needed. Hence, X-ray radiation is chosen.

X-Ray diffraction phenomenon is described by Bragg's Law which was proposed in 1913 by W.L. Bragg[6]. Bragg describes crystals as sets of planes whereas each plane consists of periodically arranged atoms with distance d. In Bragg's Law,

it was pictured that when two parallel incident rays strike two parallel planes with a distance d, the difference in path length between the two rays must be equal to a multiple of the wavelength to get a constructive interference. The path difference between the two rays is 2dsinθ and θ is the angle of incidence. The scheme of crystal diffraction can be seen in Figure 2.1. Bragg's condition is written as the following equation:

$$n\lambda = 2dsin\theta \tag{2.1}$$

where n is an integer and indicates the order of reflection. When this condition is fulfilled for one layer and the layer below it, this means that the layers with identical spacing will also fulfill this condition and contribute to the diffracted intensity[7].

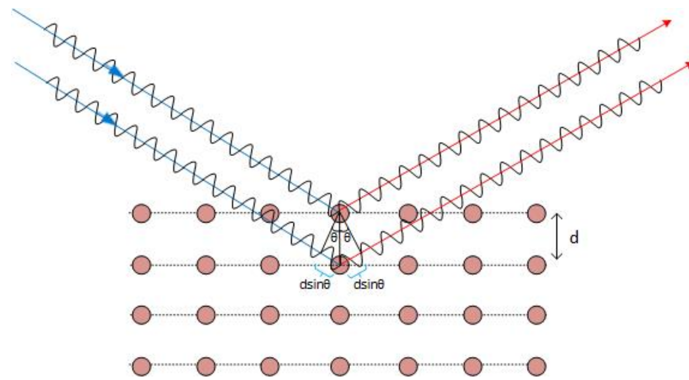

Figure 2.1: Schematic drawing illustrate Bragg condition of diffraction. Constructive interference occurs when the path difference between two rays equal to 2dsinθ

2.2 Reciprocal Space

A reciprocal lattice is a set of all vectors in a Fourier transform of a real lattice. In general, any function f(x) that is periodic in x can be represented by Fourier series and written as below

$$f(x) = a_o + \sum_{n+1}^{N} [a_n cos(\frac{2\pi n}{L}x) + b_n sin(\frac{2\pi n}{L}x)] \tag{2.2}$$

where n is integer and L is a length of the repeated distance in real space.

The potential energy U(x) that the electrons experience while moving in the lattice can also be written using Fourier series. In this case, Fourier series is

used to approximate U(x) where U(x) is written as

$$U(x) = U_o + \sum_{n+1}^{N}[c_n cos(\frac{2\pi n}{a}x) + d_n sin(\frac{2\pi n}{a}x)] \tag{2.3}$$

redefining this equation, it can also be written as

$$U(x) = \sum_{g_n} U_{g_n} e^{ig_n.x} \tag{2.4}$$

where $g_{\pm n} = \pm n\frac{2\pi}{a}$, $c_n = U_{g_n} - U_{-g_n}$, and $d_n = i(U_{g_n} - U_{-g_n})$. g_n is called as reciprocal lattice vector.

With enough series of term, exact shape of the interaction potential energy as a function of position x can be reproduced. This Fourier series guarantees translational invariance of U(x) where at a random point at a one dimensional arrangement of crystal x+ma where a is the lattice constant and m is the displacement factor, this should fulfill

$$U(x) = \sum_{g_n} U_{g_n} e^{ig_n.x} = U(x+ma) = \sum_{g_n} U_{g_n} e^{ig_n.(x+ma)} \tag{2.5}$$

The equation above will require $e^{ig_n.(ma)} = 1$ so that $g_n(ma) = 2\pi N$, where $N = nxm$ is an integer.

This translational invariance also applies for free electron wave function $\psi(x)$ which is defined by

$$\psi(x) = Ae^{ikx} = \psi_k(x) = Ae^{ig_n x} = \psi_{g_n}(x) \tag{2.6}$$

whenever $k = g_n = a\frac{2\pi}{a}$. Hence when there is a translation through a distance of l, where l=ma and m is an integer, it becomes

$$\psi_{g_n}(x+l) = \psi_{g_n}(x) \tag{2.7}$$

Thus, in real space the crystals have atom distance of a, while in reciprocal space, also called as k-space, the distance of atoms are $2\pi/a$. To generate a reciprocal lattice, three primitive vectors a_1, a_2, and a_3 are used. a_1, a_2, and a_3 are the set of primitive vectors of a real lattice as below.

$$b_1 = 2\pi\frac{a_2 x a_3}{a_1.(a_2 x a_3)} \tag{2.8}$$

$$b_2 = 2\pi\frac{a_3 x a_1}{a_1.(a_2 x a_3)} \tag{2.9}$$

$$b_3 = 2\pi\frac{a_1 x a_2}{a_1.(a_2 x a_3)} \tag{2.10}$$

2.2.1 Laue condition and Ewald's sphere

In reciprocal space, or k-space, a constructive interference happens when the change in wave vector equals to a reciprocal lattice vector[8].

$$K = k - k' \tag{2.11}$$

where K is the reciprocal lattice vector, k is the incident wave vector and k' is the diffracted wave vector, see Figure 2.2.

The condition above is called Laue condition. The Bragg and Laue formulations are equivalence whereas a Laue diffraction peak corresponds to a Bragg reflection from real lattice planes which are perpendicular to the reciprocal lattice vector K[8]. The construction of this is shown by Ewald's sphere in Figure 2.2. Ewald's sphere is a sphere in k-space that constructed with incident wave vector k and diffracted wave vector k' as its radius, where k and k' have the same length $1/\lambda$. From Bragg's law, since $|\sin\theta| \leqq 1$, hence $\lambda/2\mathrm{d} \leqq 1$. This leads to a conclusion that $|\mathrm{K}| \leqq 2/\lambda$[9]. This means that only a limited number of reflections can occur within the radius of twice of Ewald's sphere, called as limit sphere. Using larger wavelength source means a smaller volume of reciprocal space can be explored.

Figure 2.2 describes that to satisfy the Laue condition,the tip of incident and diffracted wave vectors must lie on the surface of the Ewald's sphere where a Bragg reflection occurs from the real lattice planes perpendicular to the reciprocal lattice. This condition also satisfies the Bragg diffraction condition where the wavelength of the radiation must be comparable to the atomic spacing of the crystalline sample. The hollow spots represents the planes in reciprocal space. From an origin (black spot), K=k-k' satisfies Laue diffraction condition and a constructive interference for a plane occurs. As there is a shift in detector, different k' will be constructed and eventually K will move to another point while maintaining the K=k-k'. Hence, a circle of Ewald's sphere will be constructed as the detector moves to all possible angles. Constructive interference only happens when K touches one of the plane in reciprocal space(the hollow spots).

There are three possible ways to achieve more possible constructive interference (get more hollow spots touched by Ewald's sphere). First, by moving the source, k vector will change in direction, enabling us to reach a different point of plane in reciprocal space. Second, by changing the wavelength since smaller wave-

length leads to a bigger diameter of limit sphere, hence leads to a bigger Ewald's sphere, making it possible to cover more reciprocal space spots. Third, by rotating or tilting the sample as if the reciprocal space gets dragged and different reciprocal space spots can possibly be touched by the Ewald's sphere.

When the planes of atoms diffract the light, the constructive interference produces a diffraction pattern of light spots in a regular array. The extended planes of atoms are represented by single points in reciprocal space as shown in Figure 2.3. Reciprocal space area covered within Ewald's sphere depends on the wavelength as stated earlier. The distance between the light spot in reciprocal lattice is inversely proportional to the atomic distance in the crystal.

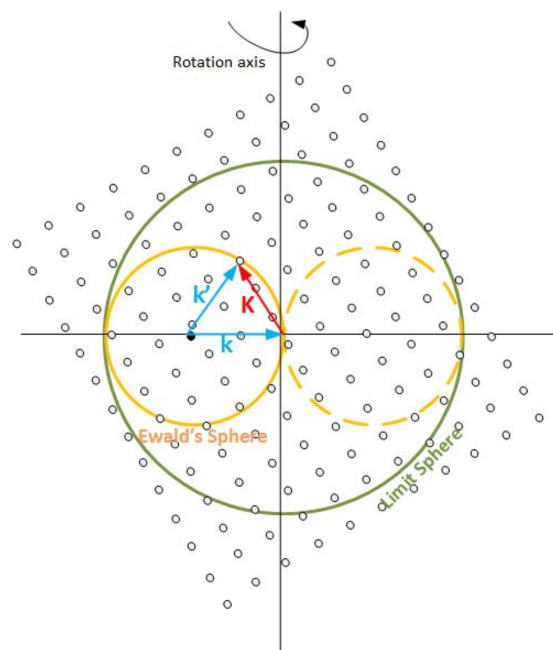

Figure 2.2: Construction of Ewald's sphere satisfying K=k-k'

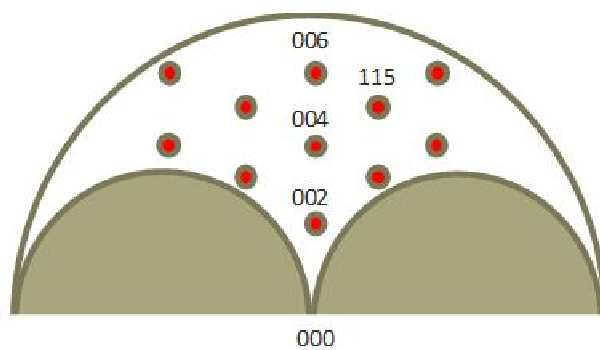

Figure 2.3: A reciprocal lattice observed within an Ewald's sphere. Red spots represents the planes of atoms in a crystal

3

Semiconductor Materials and Molecular Beam Epitaxy

3.1 Semiconductor Material

Semiconductor is a material with a bandgap ranging between those in isolator and conductor as illustrated in Figure 3.1. A band gap is the amount of energy needed to excite one electron from valence band into conduction band. In conductor the conduction and valence bands overlap with each other therefore the electrical properties of a conductor is uncontrollable. In insulator the bandgap is huge which means a huge amount of energy is needed to create charge carriers. This leads to a difficulty for charge carriers to flow in insulator. In a semiconductor, the bandgap is quite narrow. With electrical or optical pump, the electrons can be excited from the valence band to the conduction band. Furthermore, the band gap of a semiconductor compound can be tuned by changing the compositions. Engineering electronic energy bands using different compound semiconductors are essential to many solid state device applications including semiconductor lasers, solar cells and transistors.

Semiconductor materials can be elements or compounds from group IV of the periodic table and also can be binary compounds that are formed by the elements of groups III-V, II-VI or IV-VI. The most well known semiconductor material of Group IV is Silicon (Si) and Germanium (Ge) which are known to have the diamond structure. Ashcroft and Mermin refer the diamond structure as ”two interpenetrating face-centered cubic (FCC)”[8], shown in Figure 3.2(a).

Another two interpenetrating FCC structure called as zinc blende struc-

ture. This structure differs with diamond as zinc blende structure composed of two constituent elements, instead of one element as in diamond structure, as shown in Figure 3.2. Some compound semiconductors such as SiC, GaAs, InAs and InP feature this structure[7]. Diamond and zinc blende structures have cubic symmetry with a=b=c and α, β, and γ are all equal to 90° where α, β, and γ are the angles between the axis. The two interpenetrating FCC structures in diamond structure that are shifted by one fourth along the space diagonal with respect to each other. In short, we can describe diamond structure as an FCC lattice with basis of two atoms. In diamond structure, each atom has 4 nearest neighbors with a packing fraction of only 0.34 and considered as one of the loosest packed of all crystal structures[5].

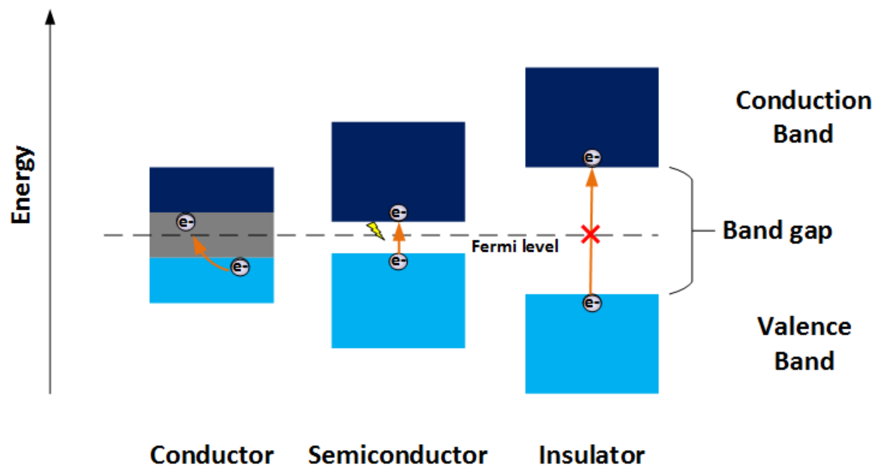

Figure 3.1: Energy bands of conductor, semiconductor and insulator

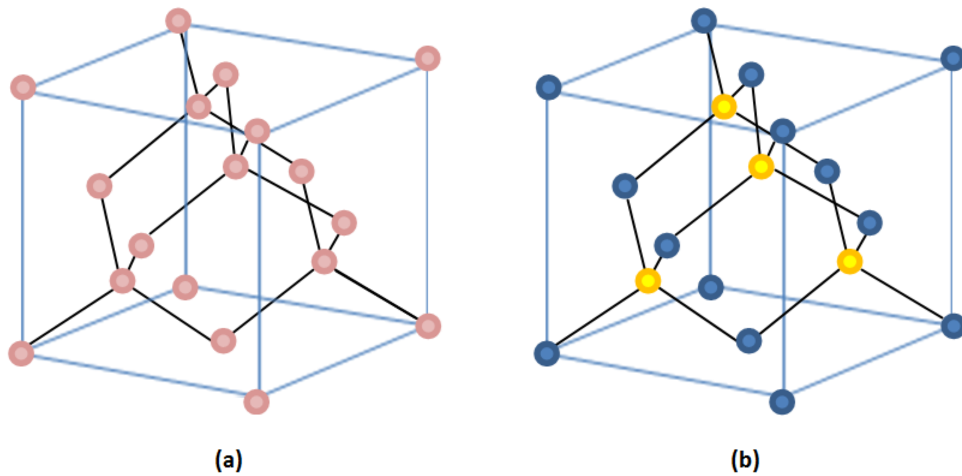

Figure 3.2: (a) diamond crystal structure and (b) zinc blende crystal structure

Other than crystals with cubic lattice, hexagonal structure is also possessed by some semiconductors. A hexagonal structure formed with a=b≠c, $\alpha = \beta = 90^o$, and $\gamma = 120^o$. In hexagonal structure, a closed packed structure called as hcp (hexagonal close-packed) is the most common structure as it is more favorable because the atoms minimum energy is low. Some elements with this hcp structure is Mg, Ti, and Be. A wurtzite structure is one type of hexagonal crystal system which composed of binary compounds. Some semiconductors featuring wurtzite structure are GaN and ZnO.

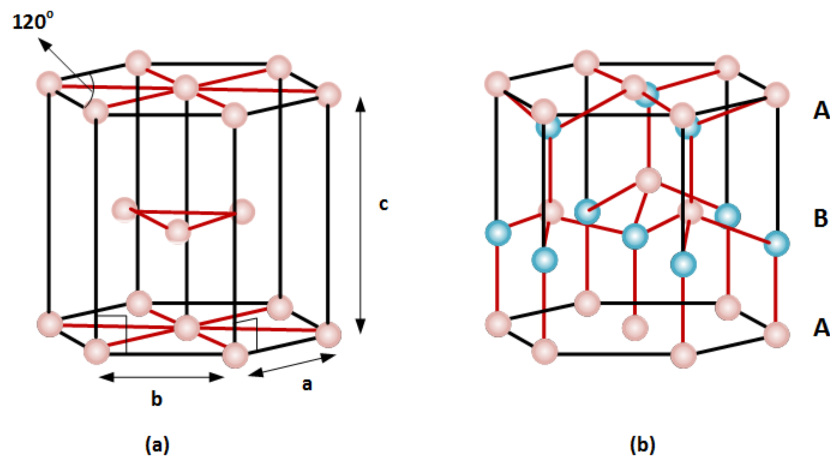

Figure 3.3: (a) hexagonal crystal structure and (b) wurtzite crystal structure

3.1.1 Lattice constant

Lattice parameter is one of the important characteristics of a material. It is defined by the unit cell size and has an important role in epitaxial materials. Figure 3.4 shows the lattice constant and energy band gap for the commonly used group IV and III-V semiconducto [10]. Table 3.1 shows a list of crystal structures, bulk lattice constants, and Poisson's ratio[11, 12].

To calculate d spacing of cubic crystal structure, below equation is used:

$$d = \sqrt{\frac{a^2}{h^2 + k^2 + l^2}} \tag{3.1}$$

with a is lattice constant, d is the spacing between diffraction planes, and h, k , and l corresponds to the hkl of the corresponding planes. The d-spacing value will be provided from our XRD measurement result. Equation 3.1 used to

calculate lattice parameter in cubic crytal structure. For hexagonal crystal structure, d spacing is calculated using equation below:

$$d = \sqrt{\frac{1}{(h^2 + k^2 + hk)\frac{4}{3a^2} + \frac{l}{c^2}}} \tag{3.2}$$

where c is the lattice parameter in out of plane direction.

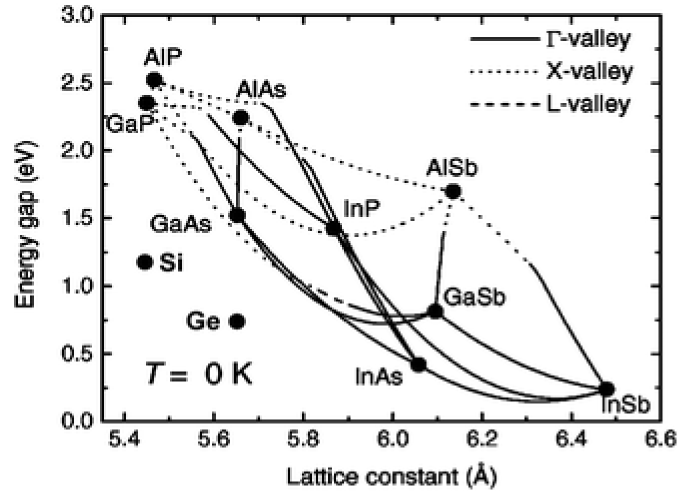

Figure 3.4: Band gap and lattice constant for various III-V and group IV material alloy

Table 3.1: Bulk lattice constant of common known materials

Material	structure	a(Å)	c(Å)	v
Si	diamond	5.43	-	0.278
Ge	diamond	5.658	-	0.273
GaAs	zinc blende	5.65	-	0.311
InAs	zinc blende	6.05903	-	0.352
InSb	zinc blende	6.46	-	0.35
ZnS	zinc blende	5.41	-	0.27
GaN	zinc blende	4.364	-	0.203
GaN	wurtzite	3.1893	5.1851	0.203
InN	wutzite	3.538	5.1851	0.203
AlN	wurtzite	3.1127	4.9816	0.24

3.2 Semiconductor heterostructures

A homojunction devices has a limitation with a fixed band structure. Thus, the carrier transport in homojunction devices can't be tuned. This had driven the researchers to move forward into the field of semiconductor heterostructure devices. The early stage of heterostructure research was in 1963 when Herbert Kroemer proposed double-heterostructure laser. He got a nobel prize in physics in 2000 for his work on the development of semiconductor heterostructures for high speed and opto-electronic application. A heterostructure devices consist of two or more layers of different materials. The different materials feature different band alignment which leads to different types of junctions depending on the materials used.

Semiconductor heterostructures are usually grown using epitaxy techniques such as Metalorganic Vapour Phase Epitaxy (MOVPE) and Molecular Beam Epitaxy (MBE). To grow different materials on top of each other, two issues have to be considered. Accurate composition control of semiconductor compounds are essential to get accurate band structures as the design And structural defects should be avoided in the active region which is deleterious to device performance. Usually a device quality heterostructure has to be grown with its lattice constant equal or close to that of a substrate to avoid deleterious structural defects. However, the types of available substrates are limited to a few numbers. Various lattice-mismatched epitaxy techniques have been developed to combine dissimilar materials for better device performances. A successful example is metamorphic high electron mobility transistors (mHEMTs)[13, 14].

3.2.1 Chemical composition

See Figure 3.4, the band gap, indicated by the dash (indirect) and solid (direct) lines, can be tuned by changing the composition of the constituent elements. In the case of $In_xGa_{1-x}As$, band gap varies between 0.36 eV to 1.43 eV while lattice parameter varies between 5.653 Å to 6.058 Å, depending on the composition of Indium and Gallium[15]. To find the composition of an alloy material $A_xB_{1-x}C$, it follows Vegards's Law where the percentages of the composition vary linearly with the lattice parameter.

In general, Vegard's Law can be written as follow,

$$a_{A_xB_{(1-x)}C} = xa_{AC} + (1-x)a_{BC} \tag{3.3}$$

where x can be calculated using

$$x = \frac{d_R - d_B}{d_A - d_B} \tag{3.4}$$

where d_R is the relaxed d spacing, d_A is the d spacing of material A, and d_B is the d spacing of material B.

3.2.2 Lattice mismatch, strain, and relaxation

Except for the chemical composition, strain also influences the lattice parameter and the band gap of the epitaxial layer film[16]. If an epilayer takes on the morphology or the lattice constant of the underlying substrate, the strained layer undergoes tetragonal distortion. As the growth of the strained material continues, a *criticalthickness* is reached beyond which the accumulated strain energy is relieved by forming dislocations. As the growth proceeds beyond the critical thickness, relaxation occurs. Relaxation implies that the material that was once strained and distorted has now come back to its original shape. In the strain relieving process the atoms skip the lattice sites and cause misfits dislocations, a source for threading dislocations, see Figure 3.5. The quality and performance of devices is degraded drastically as the threading dislocations propagate vertically into the active regions, acting as nonradiative recombination centers and current leakage paths.

Relaxation is calculated using equation below:

$$R = \frac{a_l - a_s}{a_l^R - a_s}.100\% \tag{3.5}$$

where 100% relaxation means that the epilayer is fully relaxed and takes its lattice constant to the bulk value, while 0% relaxation means that the epilayer is fully strained or in a pseudomorphic state, indicatingthat it planar lattice follows the lattice parameter of the substrate. Strain and relaxation can be extracted from XRD measurements since changes in lattice parameters result in a shift in the diffraction peak.

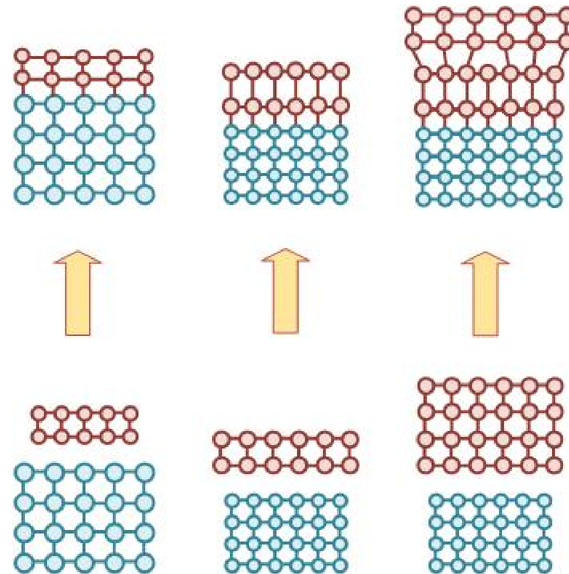

Figure 3.5: Strain and relaxation in lattice mismatched epitaxial layer on substrate. Figure on the right shows how a relaxation of strain can cause a defect in a grown layer

3.3 Molecular beam epitaxy

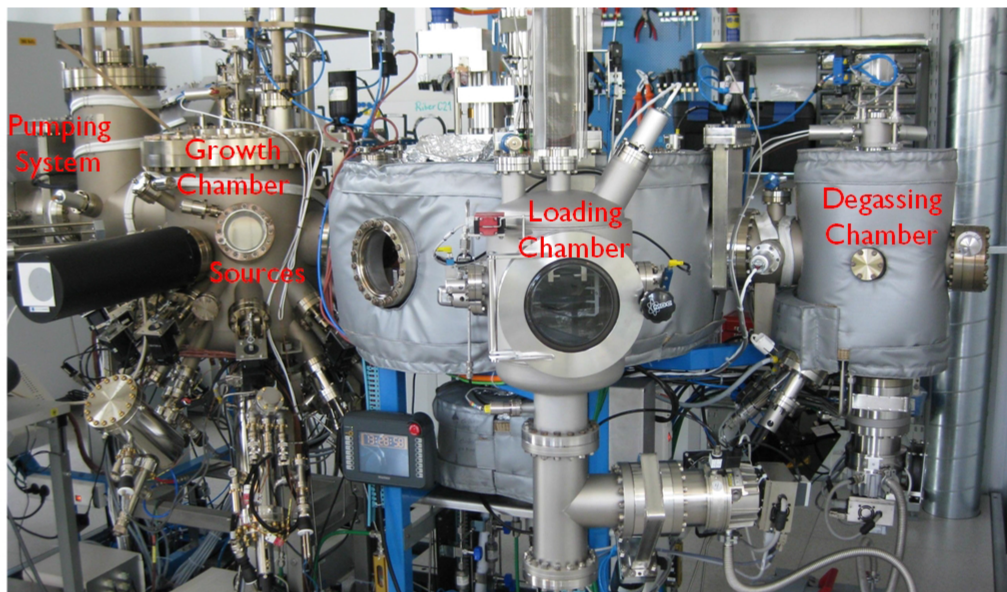

Figure 3.6: Riber Compact C21 MBE system used in this work [1]

Techniques to grow semiconductor material epitaxially has been developed since 1960s. There are several others epitaxial techniques that had been developed,

including vapor phase epitaxy, metal-organic vapor phase epitaxy, liquid phase epitaxy, and molecular beam epitaxy. Nevertheless, MBE is one technique that is favored due to its sev-eral advantages, including high purity materials (ultra high vaccum enviroment), precise control over growth rate, and the use of low temperature growth. Growth rate of MBE is ≈ 0.01 μm/min, with growth temperature ranging from 450-550 ^{o}C, and thickness control up to 5 Å[17].

Samples investigated in this thesis were all grown by MBE. These samples were prepared using Riber Compact C21 MBE system which composed of three different chambers; loading chamber, outgassing chamber, and growth chamber as seen in Figure 3.6[1]. Loading chamber is used to load and unload the substrate wafers and outgassing chamber is used to prepare the substrate by baking them before going into the growth chamber. Inside the growth chamber, substrate is mounted facing down the source. Sources were then thermally heated by Joule effect through wires. The evaporated source vapors then act the molecular beam for the growth. There is a mechanical shutter inside this chamber which helps to switch between material sources. To get better diffusion of absorbed molecules into the substrate, the temperature of substrate holder can be adjusted in accordance with needs.

4

XRD measurement

The resolutions of an X-Ray diffractometer are varied into three kinds of resolutions; low resolution, high resolution, and ultra high resolution, which is determined by the incident and detector optics used in the instrument. This chapter will discuss the instruments along with some discussions on the optic configuration, measurement methods, and scan types.

4.1 Instrumentation

In general, an X-ray diffractometer is composed of an X-ray source, incident beam optics, sample stage, and diffracted beam optics. All instrumentation parts will be discussed in this section.

4.1.1 X-ray beam source

Inside the X-ray beam source, a tungsten filament which acts as a cathode is heated by passing current to create emission of electrons. The cathode has a high negative potential while the anode is ground. This high voltage differential accelerate the electrons toward the anode. The electrons strike the anode and induce vacancies as the electrons from the inner shell of the anode atom get ejected. Electrons from higher energy level will fill up the vacancies creating photons with certain wavelength. Hence, emission of X-rays occurs. However, only about 1% of energy is converted into X-rays and 99% of it dissipates in form of heat. Due to this reason, the back of the anode is cooled with water during operation. The anode material is Cu with $K\alpha_1$ wavelength of 1.540593 nm. There are two focus types of the beam

source, namely line focus and point focus. These focuses are to be used accordingly for different types of incident beam optics.

4.1.2 Incident optics

One type of incident optics consists of a divergence slit and a hybrid monochromator. This type of incident beam optics uses line focus beam source. The divergence slit is placed 100 mm in front of the x-ray tube. It is software controlled and a fixed divergence slit mode of $1/8^o$ was used in our HRXRD measurements.

A hybrid monochromator consists of a monochromator and a mirror. The mirror is used to reshape the divergent beam of the line focused X-ray tube. It is also used to eliminate Cu Kβ lines. The monochromator that is embedded in our equipment is Ge(220) 4-bounce monochromator. A crystal monochromator is used to monochromate X-ray beam. The four crystals are set at a Bragg angle for Cu Kα_1 line. Beams with wavelength longer or shorter than Kα_1 will have different Bragg's angles, hence will be bounced out and only beam with Kα_1 can pass the monochromator. There are different types of crystal monochromators, including Ge (220) 4-bounce and Ge(440) 4-bounce. A Ge(440) will give higher resolution and more narrow wavelength in trade of its intensity. The more monochromated the light, the less intensity will come out. In this thesis, this type of incident beam optic is to be used for out of plane measurements to determine thin film parameters such as strain, relaxation, composition and layer thickness .

Figure 4.1: Hybrid monochromator used in most measurement in this work

Another type of incident beam optic used in this thesis is X-ray lens. In X-

ray lens optics, the divergent incoming beam from a point focus source is collimated into two dimensions quasi parallel beam using glass capillaries that are bent in parabolic shape which acts as a waveguide for the X-ray beam. Inside these glass capillaries, X-ray beam went through using the effect of total external reflection as illustrated in Figure 4.2. The irradiated area of sample using this lens optics depends on the position of the sample, the angle of incident, also the incident beam size. In X-ray lens the aperture of the crossed slit collimator can be adjusted. This type of incident beam optic is to be used with point focus source and a parallel plate collimator as the diffracted beam optic. This type of XRD configuration is mainly used to characterize samples with unknown composition. In our work, this configuration was used in order to find phase composition in our nanowire samples.

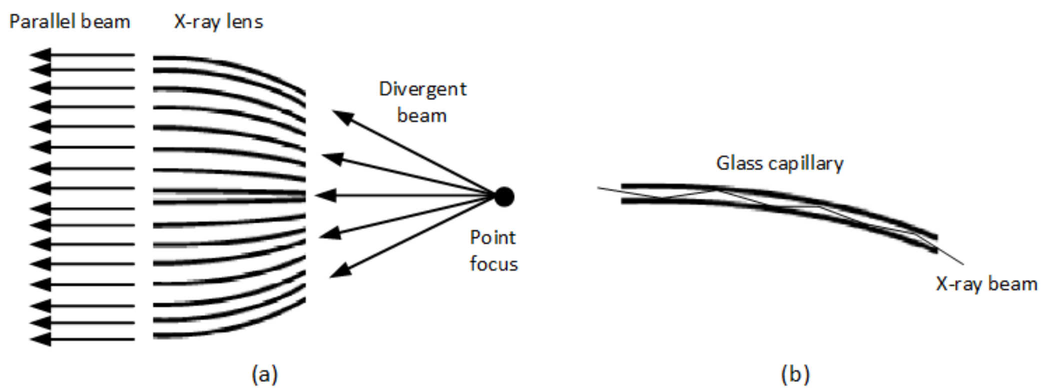

Figure 4.2: (a) schematic of X-ray lens and (b) total reflection inside glass capillary

Figure 4.3: X-ray lens incident beam optic used in this work

4.1.3 Sample stage

PANalytical X'Pert diffractometer is equipped with a sample stage attached to a goniometer which makes it possible for higher precision of sample position by eliminating error in ω and 2θ axis alignment[18]. Other than the main axis ω and 2θ, the movement of sample stage in χ axis, ϕ axis and x, y, and z direction can be controlled using embedded software. χ axis is a tilt axis that can move up to 180° and ϕ axis is a rotation axis that can rotate 360°. The associated movements of sample stage are shown in Figure 4.4.

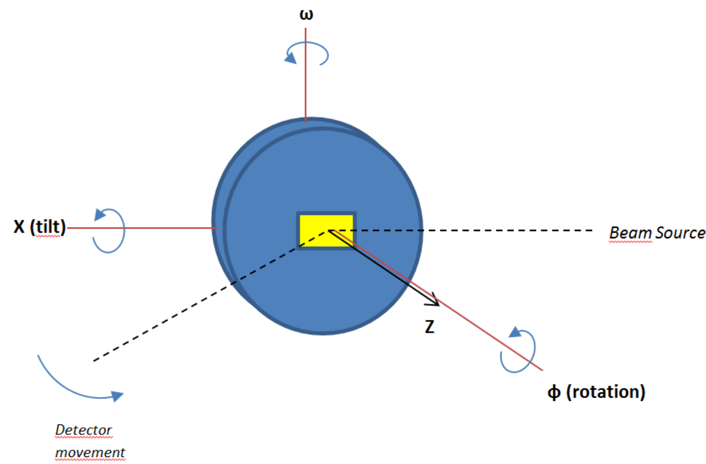

Figure 4.4: Schematic of sample stage movements

4.1.4 Diffracted beam optics

In our measurement, a Pixcel 3D detector is used as the diffracted beam optic for HRXRD measurement. This detector has different modes that can be used, including scanning and static area detector mode, scanning and static line detector mode, open detector mode, and receiving slit mode. Different mode of measurement is intended for different use and they have different characteristics. In the receiving slit and open detector mode, it is possible to do omega, 2theta, omega-2theta, 2theta-omega, phi, chi, x, y, and z scans. In the scanning line mode, the possibility of scan axis decreases into 2theta, 2theta-omega, and omega-2theta. In the static line mode, the scan axis possible is only 2theta. In receiving slit and open detector

mode, the smallest step size is 0.0001^o while the time/step is not limited, while in scanning line, the smallest step size is 0.0012310.

Receiving slit and open detector mode are the only possible mode to do proper alignment using Pixcel detector. In the alignment process, the ability to scan phi, chi, and z axis is crucial to get the highest possible intensity. A detail discussion on alignment process is listed in Appendix B. However, to get the final result, despite of the impossibility to be used in alignment, scanning line mode gives several advantages over the others. With scanning line mode, much faster measurement with much higher resolution can be done. As a comparison, take a look at table 4.1. The same resolution can be achieved with scanning line measurement much faster than receiving slit. This is possible because in scanning line mode, the detector scans 255 points simultaneously, compared to one point at a time with receiving slit. This feature is especially useful for RSM scan which could take hours even if scanning line detector mode was being used.

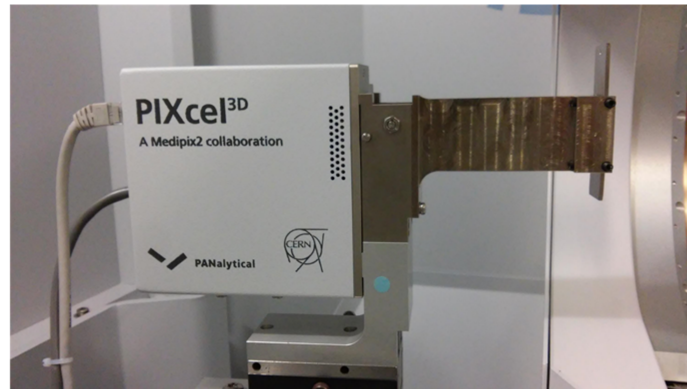

Figure 4.5: Pixcel 3D detector

Table 4.1: Comparison on Receiving slit and Scanning line

Type of scan	range(^{o})	step size(^{o})	time/step	total time
Receiving slit	6	0.01	0.5	5 minutes
Receiving slit	6	0.001	10	18 hours
Scanning line	6	0.0012310	10	5 minutes

In the static line mode, the scan axis is only limited to 2theta. The scanning range is limited to 2.5108^o and step size of 0.0098461^o. The static line mode differs compared to other types of scans where in other modes scans are done continuously

but in the static line mode, scan is done in a static way, where in this mode detector and omega fixed in one positions and detector will collect all intensity gathered in an amount of time and only time/step can be changed while range is defined by the active length. Figure 4.6 shows a 2.5108 range of 2theta measurement with step size of 0.0098461 for time/step of 20 and 30 sec. The total time are 30 sec and 40 sec, respectively.

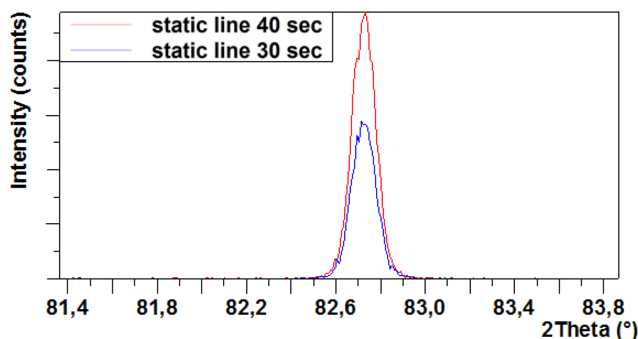

Figure 4.6: Static line mode (115) 2theta measurements of an InAs sample for different amount of measurement time

Another type of diffracted beam optic used is parallel plate collimator. The parallel plate collimator is used to define the equatorial acceptance angle of the diffracted beam as seen by the detector. The parallel plate collimator consist of parallel plate with direction perpendicular to the diffraction plane. The detector itself can be attached and reattached to this optic separately. This type was used in configuration with X-ray lens as the incident beam optics. As in high resolution XRD where RSM was done to make sharp peak, X-ray lens configuration can also be used in RSM measurement to show the spread of d values and angles in misoriented crystallites.

Figure 4.7: Parallel plate collimator used in X-ray lens configuration

4.2 Instrument configurations, measurement methods, and scan types

There are two configurations used in this work. Both will be discussed along with the measurement and scan types in this section.

4.2.1 Configuration types

4.2.1.1 HRXRD

Figure 4.8 shows the detail configuration of the HRXRD optic system used in our measurement. In this work, HRXRD was used to characterize all samples. With this configuration, X-ray tube was in line focus, incident beam optics were divergence slit and hybrid monochromator, and diffracted beam optic was Pixcel 3D.

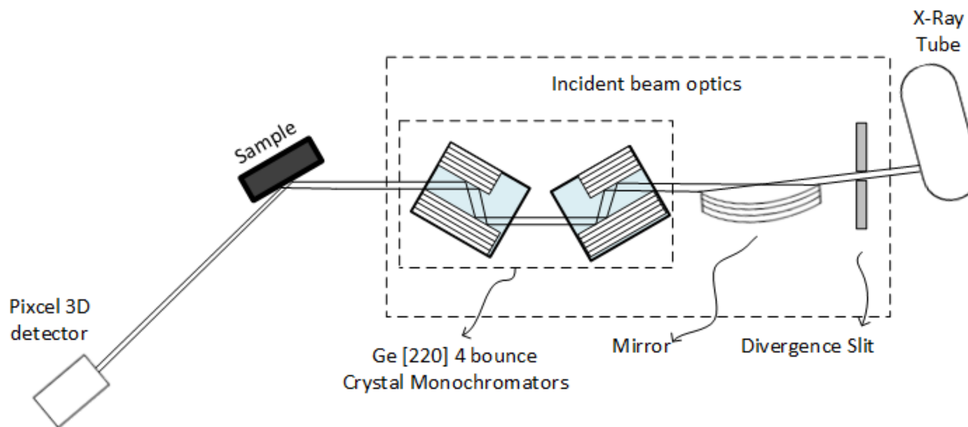

Figure 4.8: High resolution XRD diffractometer configuration

4.2.1.2 X-ray Lens

Figure 4.13 shows the detail configuration of the X-ray lens optic system used in our measurement. In this work, X-ray lens configuration was used to characterize nanowire samples. With this configuration, X-ray tube was in point focus, incident beam optics X-ray lens, and diffracted beam optic was parallel plate collimator.

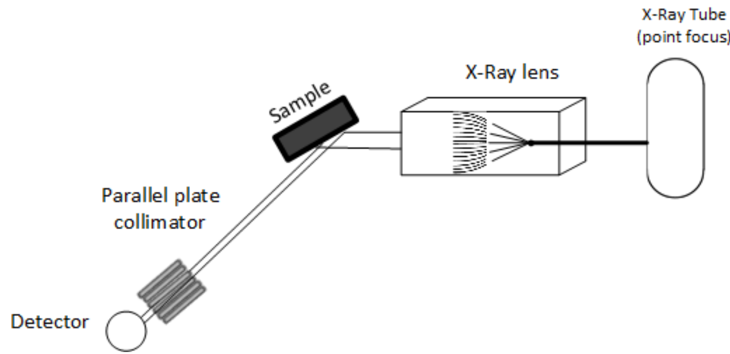

Figure 4.9: X-ray lens configuration

4.2.2 Measurement types

There are different types of measurements that can be conducted with this device; namely out-of-plane measurement, in-plane measurement, and X-Ray reflectivity measurement.

4.2.2.1 Diffraction planes

We will discuss about diffraction planes before discussing the mentioned measurement methods, since for any measurement a diffraction plane has to be selected. The diffraction planes can be classified to be symmetric plane and asymmetric plane. The geometry of symmetrical and asymmetrical out of plane diffraction is illustrated in Figure 4.10. The angle between diffraction plane and incident angle is ω, while the diffracted angle is 2θ. Symmetrical planes are the planes that are parallel to the surface of the sample, while asymmetrical planes are the planes that have an angle to the surface of the sample (obtained by tilting the sample) as in Figure 4.11.

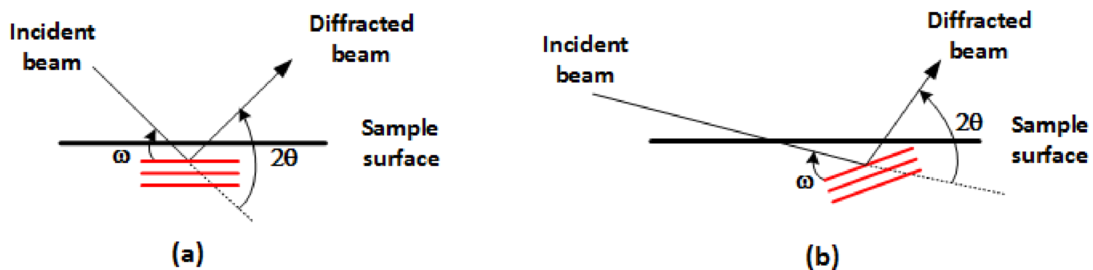

Figure 4.10: Geometry for (a)symmetrical and (b)asymmetrical out of plane diffraction

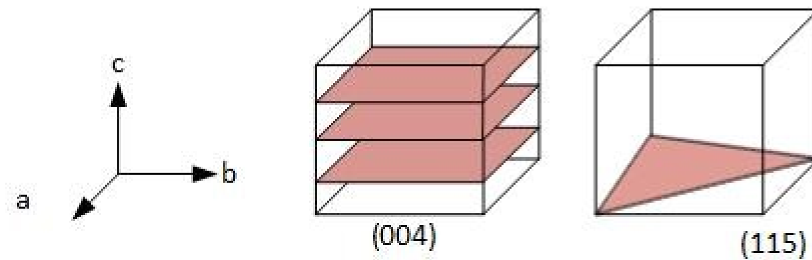

Figure 4.11: Examples of symmetric and asymmetric crystal planes

4.2.2.2 Out of Plane Measurement

Out of plane measurement system is as seen in Figure 4.12.

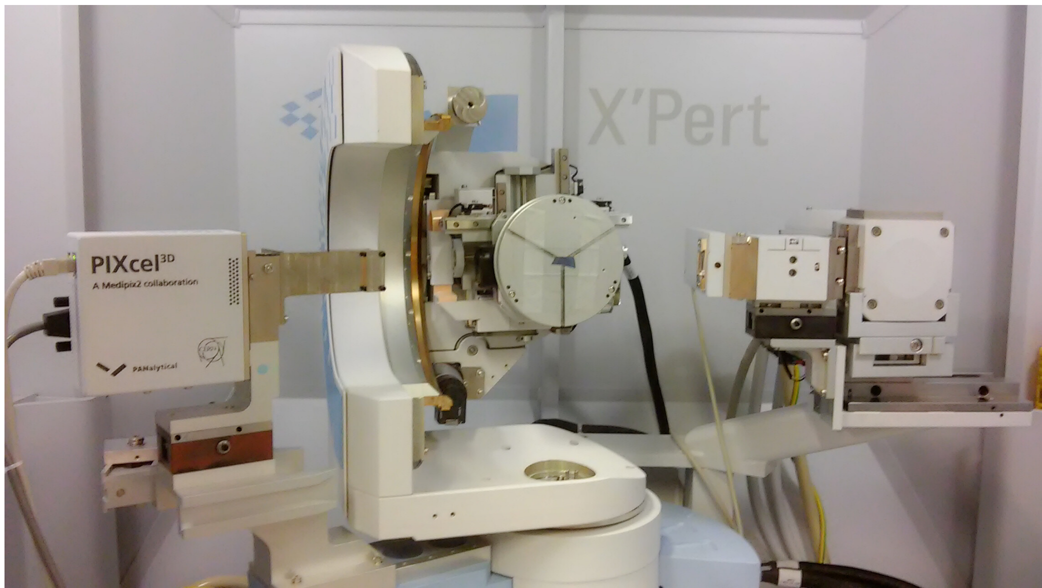

Figure 4.12: Out of plane XRD configuration

Out of plane measurement is the most commonly used measurement method. For out of plane measurement, the penetration depth of the X-ray can be considered as deep penetration, leading to diffraction peaks from both substrate and epilayers. The substrate peak is usually very strong and covers the weak epilayer peaks. Generally, asymmetric plane measurement is more favorable because the angle of incidence with respect to the sample's surface is smaller than symmetrical plane measurement hence the penetration depth is smaller, leading to higher diffraction intensity from the epitaxial layer. Calculated penetration depth for symmetrical and asymmetrical reflection for Si(111) are 38.4 μm and 2.7 μm (at $\alpha = 0.5^o$) respectively[19].

Symmetrical and asymmetrical scans are both needed to be able to find different properties of materials. Symmetrical scans only provides information about in plane (parallel) lattice parameter. As conducted in this work, symmetrical plane measurement was used to find the tilt of the epitaxial layer, while asymmetrical plane measurement was used to find lattice mismatch, strain, and relaxation.

4.2.2.3 In Plane Measurement

In the case of very thin epitaxial layer sample, the diffraction intensities from substrate and epitaxial layer can have a huge difference, because of the small volume of epilayers compared to that of the substrate. In plane measurement deals with this problem as it uses a grazing incidence, meaning that it uses a really small incidence angle, which will control the penetration depth of the source light, hence the intensity from the substrate can be limited and the intensity of the epitaxial layer can be maximized.

In plane measurement set up is shown in Figure 4.13[20]. What differs between out of plane and in plane measurements are the goniometer positions which rotated 90° and chi is on 90°. For this scan, the incidence angle must be larger than the critical angle of the material to avoid full reflection. For silicon, the critical angle is 0.23^o[21]. The most common configuration to do in plane measurement is using x-ray lens as incident beam optics and parallel plate collimator as diffracted beam optics. Both RC and RSM scans can be done with this measurement as well.

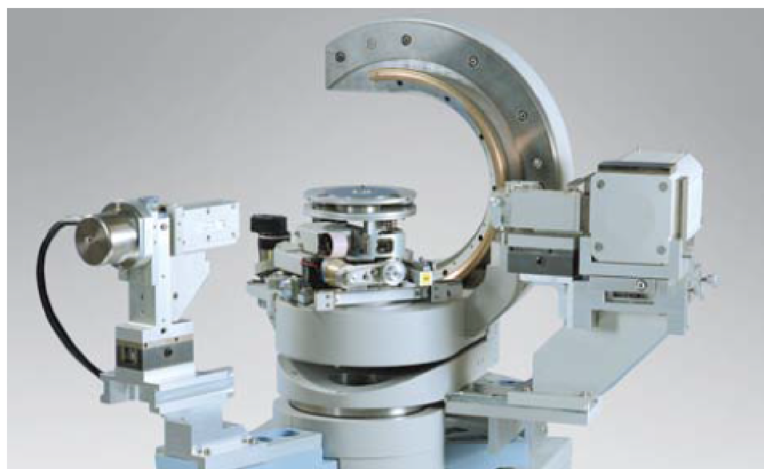

Figure 4.13: In plane XRD measurement set up

Another important characteristic of this method is that instead of measuring lattice planes that are nearly parallel to the surface in out of plane measurement, this scan measures diffraction from the planes that are nearly perpendicular with the surface, see Figure 4.14. The penetration depth of in plane diffraction is limited to less than 100 nm from the surface.

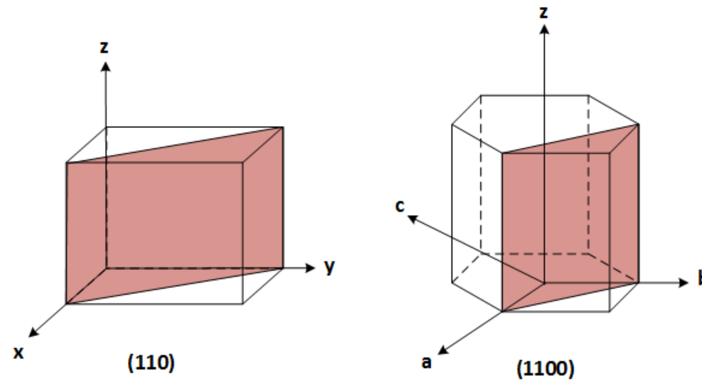

Figure 4.14: Illustration of perpendicular lattice planes in cubic and hexagonal lattice

4.2.2.4 X-Ray Reflectivity Measurement

XRR can be used to determine the thickness and density of the material, and the roughness of a material surface. To do XRR, the incidence angle must be below the critical angle for the light to be completely reflected. XRR can be used for single crystalline, polycrystalline, or amorphous material. With XRR, a thickness up to tens of nanometers can be measured.

Figure 4.15 shows XRR results directly taken from [22]. Determination of sample thickness is done by calculating the distance between the fringes. The distance between the fringes is inversely proportional to the thickness of the layer, i.e. for a thicker film, the oscillation period will be shorter. The amplitude of oscillation along with the critical angle give information about the density. Roughness information can be obtained by looking at the decay of intensity. A rougher surface will cause a lot faster decay of intensity. This is due to the fact that a rougher surface scatters light more than reflecting it. Applicable film thickness to be measured using XRR is from tens of μm up to hundreds of μm depending on used incident beam optics[22].

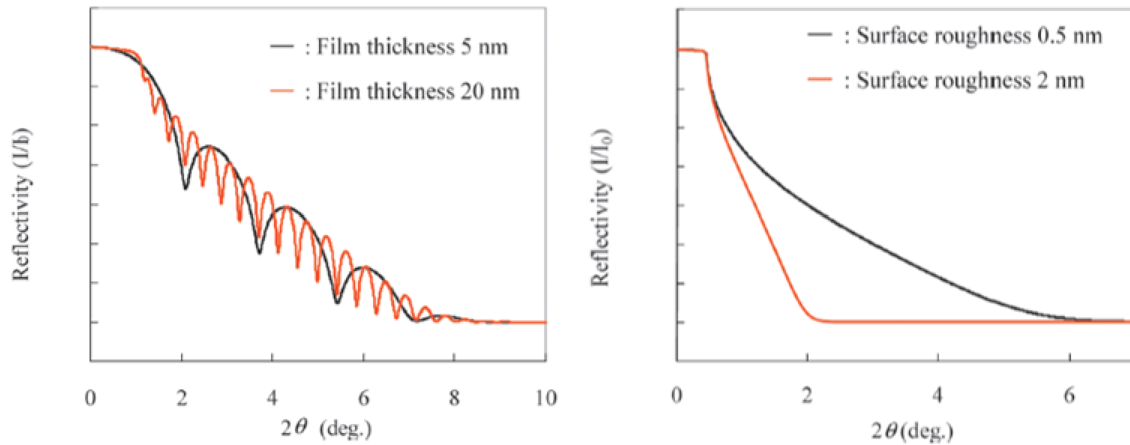

Figure 4.15: XRR results giving information about thickness and surface roughness

4.2.3 Scan types

4.2.3.1 Rocking curve

This type of scan usually come by different names depending on the output and the movements of the instrumentation. There are three types of rocking curve scan, as follows:

1. Rocking curve or omega scan
   In this scan, the sample is tilted while the detector is set in an angle (only omega changes). The result is a plot of X-ray intensity vs omega.

2. Detector scan or 2theta scan
   In this scan, the source is fixed and only the detector that moves (only 2theta changes). The result is a plot of X-ray intensity vs 2theta.

3. Coupled scan or omega-2theta scan or 2theta-omega scan
   In this scan, the source is fixed, but if sample rotates, the detector also rotates (2theta=2omega+offset).

All three types of scan are shown in Figure 4.16. Notice that for omega and 2theta scans (graph (a) and (c)), the two peaks have different colors. This is

because for omega and 2theta scans, two measurements needed to be done to get both substrate and epilayer peaks which are done by setting different 2theta (in omega scan) or omega (in 2theta scan) with different offsets. In omega or 2theta scans, the offset changes as the scan goes- Therefore, the two diffraction peaks could not be obtained with one measurement. While in coupled scans (graph (b) and (d)) it is possible to get both peaks because the offset stays the same throughout the measurement. Omega scan and 2theta scan are needed in the alignment process. More detailed procedure on sample alignment is listed in Appendix B. Alignment is crucial to get high intensity and high resolution diffraction result, because offset will not be exactly as in theory due to the imperfect mounting of the sample and also due to tilt. Although, for time efficiency, coupled scan is usually used to show the final result.

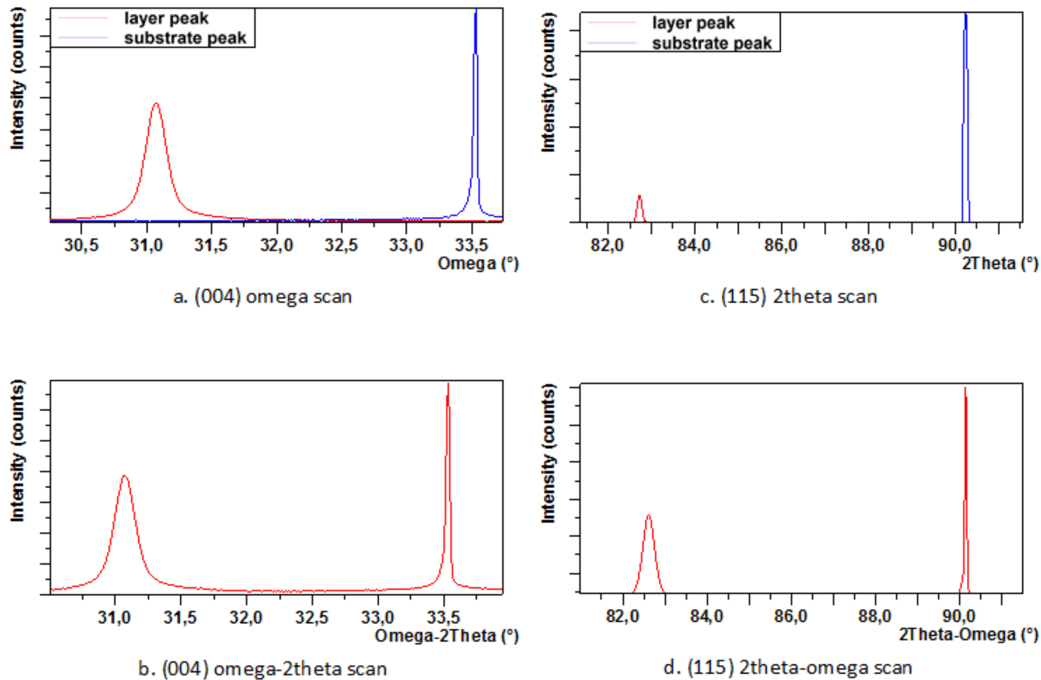

Figure 4.16: Out-of-plane rocking curve measurements of an InAs film grown on GaAs substrate (a) (004) omega scan, (b) (004) omega-2theta scan, (c) (115) 2theta scan, and (d) (115) 2theta-omega scan

With rocking curve scan, each peak indicates different ω and 2θ. This ω and 2θ data will be then used in calculations to find the properties. Qualitatively, the determination of the quality of crystal can be taken based on the FWHM of the peaks. A perfect crystal will have a very sharp peak. A broadening of the curve can be related to the presence of mosaicity, dislocation, or curvature in the sample.

From the peaks Bragg angle, qualitatively different composition of samples can be seen by the shifting of the peak. Shifts of peak to a bigger or smaller Bragg angle will depend on the lattice constants of the composed materials. Using RC, thickness can also be calculated by observing the fringes oscillation period and peak positions. Generally, a thicker film leads to smaller oscillation frequency.

4.2.3.2 Reciprocal Space Mapping (RSM)

In both out of plane and in plane measurement, a 2-axis scan called as Reciprocal Space Mapping can be made. With regular $\omega-2\theta$ or $2\theta-\omega$ rocking curve scans, both peaks from substrate and layer can be obtained with the requirement that both have the same omega offset. Omega offset is the angle of the plane to the normal of the surface. With RSM, for example with 2θ as x axis and ω as y axis, it scans a range of 2theta for one step of omega. Hence, other peaks with different omega offsets than the substrate can also be observed. From the peaks of RSM scan, calculation of tilt, strain, mismatch, and relaxation is possible to be done. RSM scan enables us to interpret data in reciprocal space.

There are several different things that we can do with RSM. It can display multiple, single, extracting and projecting maps, and extract line scans. Based on the peak positions and layer substrate peak separation, d spacing, parallel perpendicular mismatch, layer thickness, and layer relaxation can be calculated. Also, in RSM it is possible to choose different intensity levels; linear, square root, logarithmic, and manual as shown below in Figure 4.17.

With RSM measurement, the graph can be presented either in angular coordinates or in reciprocal lattice coordinates. Angular coordinates RSM is as shown in Figure 4.18(a). The x and y axis can be omega, 2theta, omega-2theta, or 2theta-omega. Reciprocal coordinates RSM shows the graph in reciprocal lattice unit Qx and Qy as shown in Figure 4.17, where Qx and Qy can be defined with the following equations.

$$Qx = R(cos\omega - cos(2\theta - \omega)) \tag{4.1}$$

$$Qy = R(sin\omega - sin(2\theta - \omega)) \tag{4.2}$$

where R is $1/\lambda = 0.6491$. Hence, the diffraction vector Q is then defined by the following equation

$$Q = \sqrt{Qx^2 + Qy^2} \tag{4.3}$$

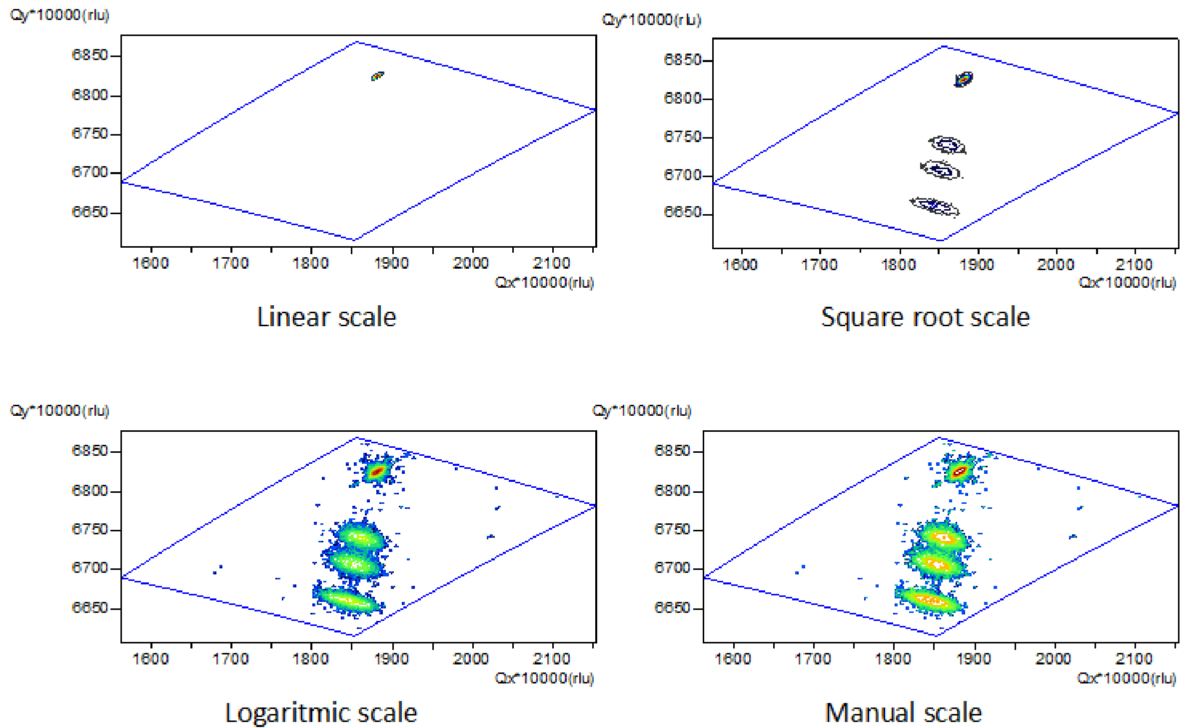

Figure 4.17: RSM example on different intensity scales

From our RSM result, a projection in x and y axis can be obtained. A projection in x and y axis of an RSM graph is a graph of added intensities from all data points with the same x and y coordinates in x and y axis, respectively. With this, all intensities with no loss can be obtained. Figure 4.18 show an example of x-axis projection from an RSM result. With the integrated intensity of adding all intensities, hence reduce the difference between substrate and layer peaks enables us to differentiate peaks better.

Analysis of material properties using RSM can be done both qualitatively and quantitatively. Figure 4.19 shows an illustration of how the position of layer peak with respect to substrate peak can give a qualitative description of its properties. Qualitatively, a symmetric RSM scan shows whether our sample is tilted or not, see Figure 4.19(a). However, to determine whether our sample is strained or relaxed, an asymmetric scans is needed, as discussed before, as shown in Figure 4.19(b) and (c). A fully strained epilayer adapts its planar lattice fully with the planar lattice of the substrate.

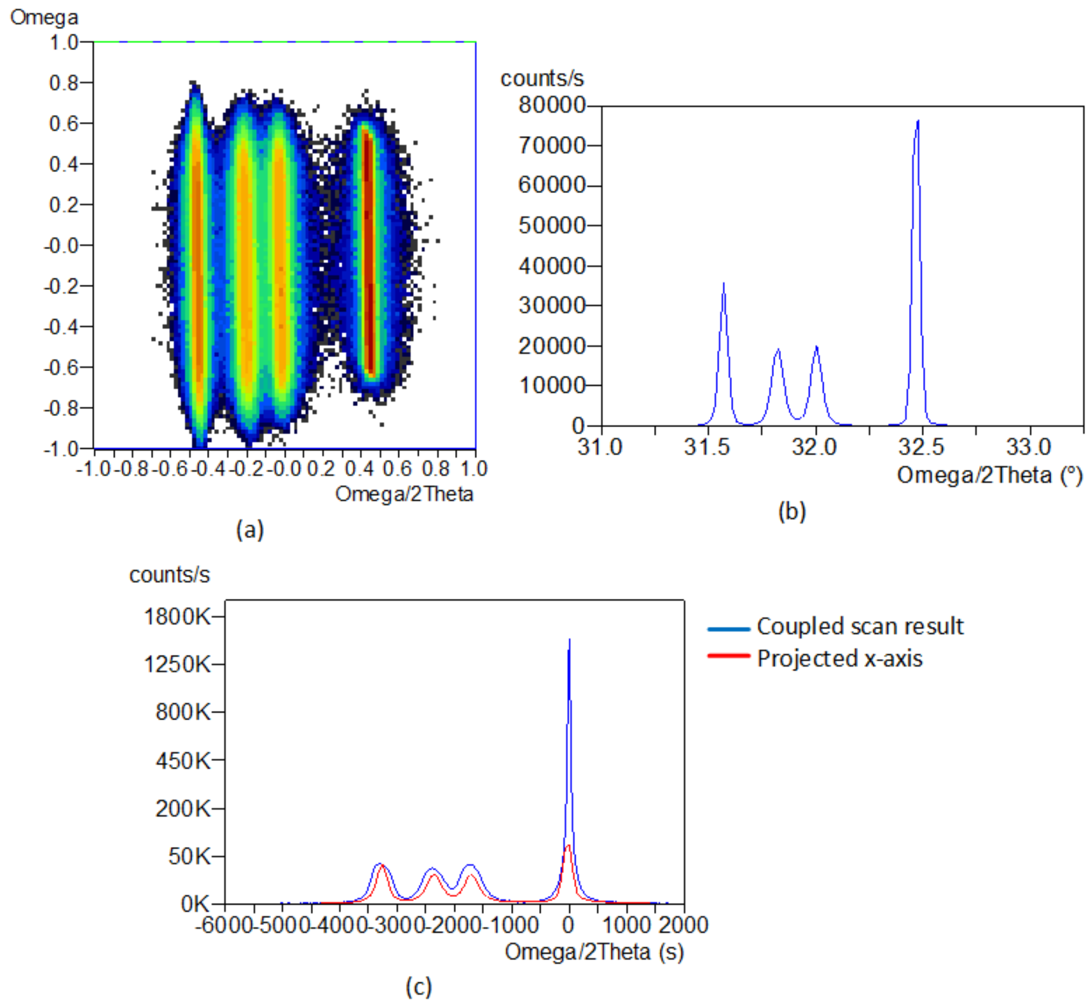

Figure 4.18: (a)RSM in angular coordinates mode, (b)RSM projection into x-axis, and (c)Projected x-axis combined with omega-2theta coupled scan result

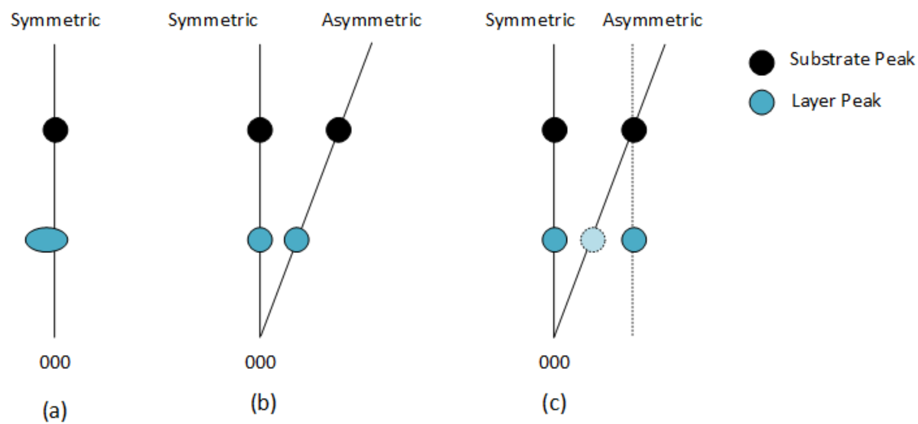

Figure 4.19: Schematic drawing explains RSM data analysis for (a)tilt seen from a symmetric scan, (b)fully relaxed layer, and (c)fully strained layer

4.3 Summary

Below is the summary of different configurations, measurements, and scan types that can be used for different purposes.

Table 4.2: FWHM comparisons of X-ray lens and HRXRD RSM results

Parameter	Configuration	Measurement	Scan
Composition	HRXRD	Out of plane	RSM
	X-Ray lens	Out of plane	RSM
Strain and Relaxation	HRXRD	Out of plane	RC (asymmetric scan)
			RSM (asymmetric scan)
	X-Ray lens	Out of plane	RC (asymmetric scan)
			RSM (asymmetric scan)
Thickness	HRXRD	Out of plane	RC
			RSM
	XRR		
Tilt	HRXRD	Out of plane	RC (symmetric scan)
			RSM (symmetric scan)
	X-Ray lens	Out of plane	RC (symmetric scan)
			RSM (symmetric scan)
Surface roughness	XRR		
Mosaic spread	HRXRD	Out of plane	RSM
	X-Ray lens	Out of plane	RSM
Curvature	HRXRD	Out of plane	RSM
	X-Ray lens	Out of plane	RSM

5

XRD Measurements on Thin Film Samples

There are two samples that will be discussed in this chapter. One is a 1.5 μm thick InAs film and another consists of three $In_xGa_{1-x}As$ films with different In compositions (three variations of unknown x), both were grown on GaAs substrates. Both Rocking Curve (RC) coupled scans ($\omega - 2\theta$ scan) and RSM scans were performed on these two samples. Two methodologies were used to extract the material properties and the results will be compared and discussed.

5.1 InAs film on GaAs substrate

The compound semiconductor InAs has a narrow band gap and a small effective electron mass, which makes it an important material in applications such as infrared detectors and high-speed electronics . In some cases, the device performance requires insulating substrates. However, semi-insulating (SI) or high resistivity InAs or GaSb substrates are difficult to produce due to their narrow band gap nature. Hence, considerable effort has been devoted to grow InAs films on GaAs and other commonly used substrates. But the large lattice mismatch between InAs and heterogeneous substrates leads to numerous dislocations, thus growth of high quality InAs films is challenging[23]. Here a sample with 1.5 um InAs grown on GaAs substrate was characterized using the out of plane configuration to investigate the residual stain.

5.1.1 Measurements and results

Both RC ($\omega - 2\theta$ scan) and RSM scan were performed using HRXRD. For this sample, four RC $\omega - 2\theta$ scans were done for symmetric (004) and asymmetric (115) planes with both $\phi = 0^o$ and $\phi = 180^o$ orientations. Measurements from different azimuths will provide the average value of tilt if a tilt is present, the angle of incident (ω) difference between substrate and epilayer will be influenced by the tilt whilst diffracted angle θ will remains, where

$$\delta\omega^{sym}_{\phi=0and\phi=180} = \delta\theta \pm \delta\gamma \tag{5.1}$$

where ω is the incident beam angle, θ is half of the diffracted beam angle, and γ is defined as tilt. These are needed to extract the residual strain. RSM scan was done for one symmetric (004) and one asymmetric (115) scan. HRXRD RC results are shown in Figure 5.1 and tabulated in table 5.1 while the RSM scan results is shown in Figure 5.2 and tabulated in table 5.2.

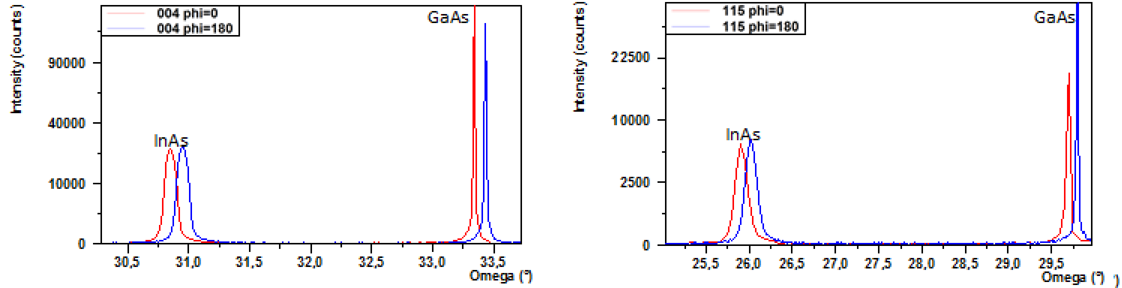

Figure 5.1: Symmetrical and asymmetrical RC peak shift between $\phi = 0^o$ and $\phi = 1800^o$ due to tilt. Tilt will cause a change in peak splitting $\delta\omega$ between substrate and epilayer when it is seen from different azimuths

Table 5.1: Data from RC scan $\omega - 2\theta$ scan

Plane	ϕ (^{o})	$\omega_s(^o)$	$2\theta_s(^o)$	$\omega_l(^o)$	$2\theta_l(^o)$
004	0	33.59864	66.08889	31.10964	61.11088
	180	33.15635	66.1849	30.65056	61.17332
115	0	29.7957	90.13855	26.10455	82.5791
	180	29.4433	89.99641	25.66703	82.44386

where ϕ is the scan azimuth, ω_s and $2\theta_s$ are the incidence angle and the diffracted angle for substrate respectively. S and l indicate substrate and epilayer peaks, respectively.

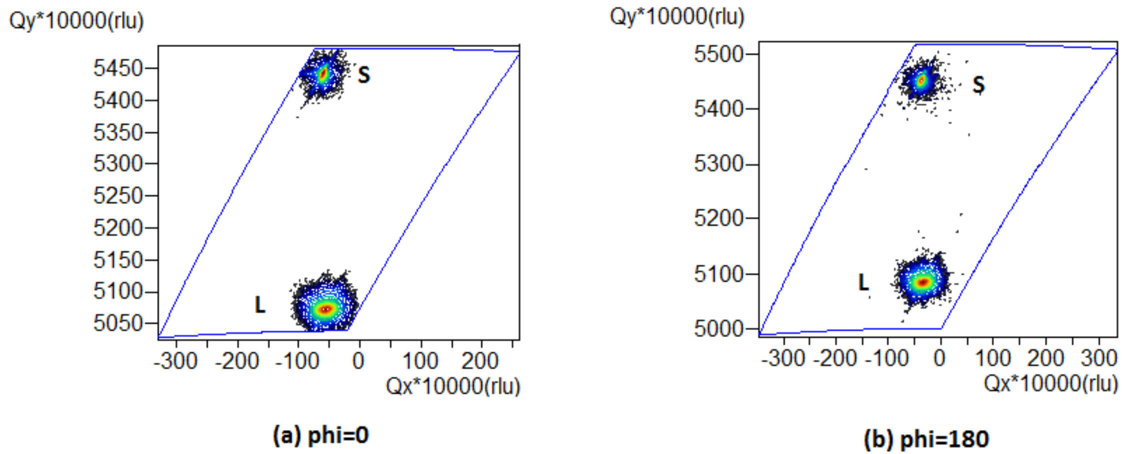

Figure 5.2: RSM (004) of InAs on GaAs at (a)$\phi = 0^o$ and (b)$\phi = 180^o$

A summary of the RSM scans results is as shown in Figure 5.3

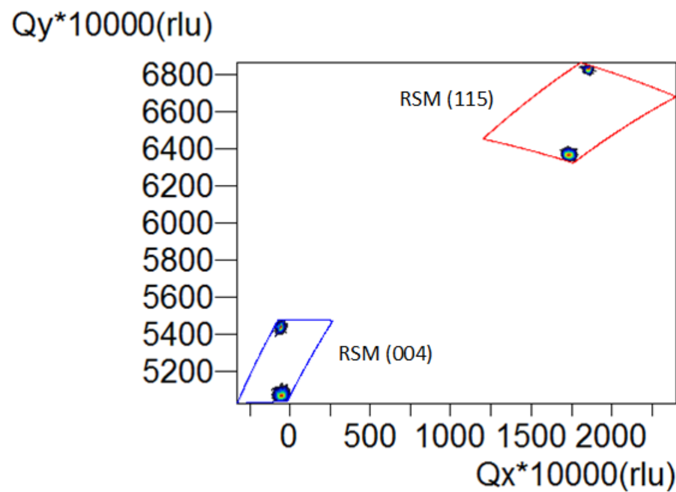

Figure 5.3: Summary of RSM scans of both (004) and (115) in one RSM graph

where ω and 2θ are the incident angle and diffracted angle respectively. Qx and Qy are the values in reciprocal lattice unit(rlu). S and L indicate substrate and epilayer peak respectively. These values can be calculated manually using equation 4.1 and 4.2, if not by the software.

Table 5.2: Data from RSM scans of InAs on GaAs sample

Plane	Phi(^{o})	Label	ω(^{o})	2θ(^{o})	Qx(rlu)	Qy(rlu)
(004)	0	S	33.61000	65.95208	-0.006022	0.544255
		L	31.11000	60.95929	-0.005580	0.507202
(004)	180	S	33.44	66.09980	-0.005713	0.545357
		L	30.95	61.10701	-0.005518	0.508331
(115)	0	S	29.88000	90.14969	0.185576	0.683277
	0	L	26.08000	82.58665	0.173170	0.636788

5.1.2 Calculation method

The residual strain can be extracted from either the RC result or the RSM scans result.

5.1.2.1 Calculation from RC result

With RC results, tilt, parallel and perpendicular average lattice constants, mismatches , strain, and relaxation of our sample can be found. Step by step calculations are as follows:

1. To find the lattice constant in perpendicular direction, calculation can be done directly using equation 3.1. While to find the lattice constant in parallel direction, we need to have knowledge on the strain in parallel direction and lattice constant in relaxed state. Relaxed lattice constant is usually known. In InAs case the relaxed lattice constant is 6.0583 Å. Strain in parallel direction will be obtained after several calculation steps described below.

2. To check the tilt, two symmetrical scans with 180° difference in azimuths are needed. Here, (004) RC scans with $\phi = 0^o$ and $\phi = 180^o$ are selected. Tilt can be calculated by using the following equation

$$\delta\gamma = \frac{(\delta\omega^{sym}_{\phi=0} - \delta\omega^{sym}_{\phi=180})}{2} \tag{5.2}$$

3. To find the difference in Bragg angle between substrate and layer, using two symmetrical RC so that the effect of tilt will be taken into account using

equation

$$\delta\theta = \frac{(\delta\omega^{sym}_{\phi=0} + \delta\omega^{sym}_{\phi=180})}{2} \tag{5.3}$$

4. To find strain and relaxation, the parallel d-spacing($d_{\parallel}$) and perpendicular d-spacing($d_{\perp}$) of the strained layer are needed. To find this, symmetrical RC will not give us the information, while asymmetrical RC will. A strain will change d_{hkl} in asymmetrical measurements with different azimuths as illustrated below in Figure5.4.

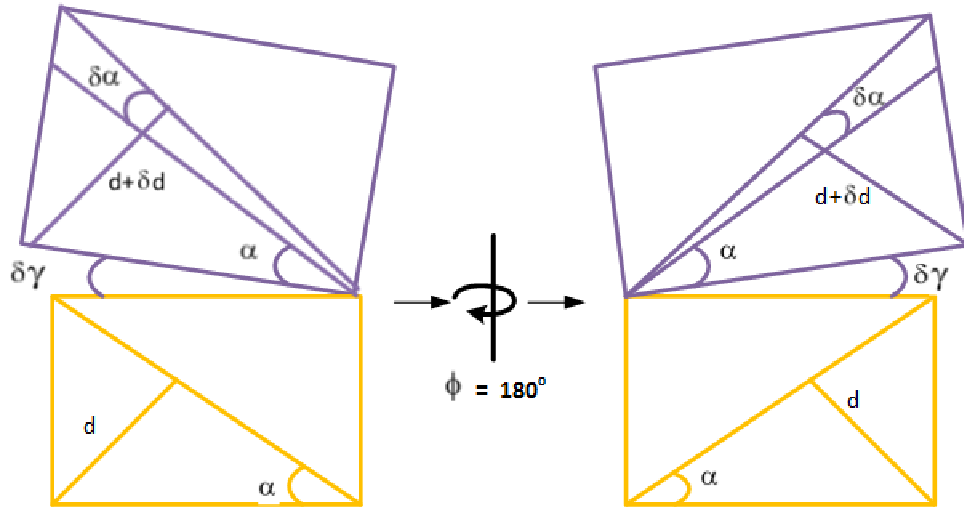

Figure 5.4: Parameters that changes due to strain in lattices at $\phi = 0^o$ and $\phi = 180^o$

5. A change in offset due to strain $\delta\alpha$ can be calculated using two asymmetrical scans (115) with $\phi = 0^o$ and $\phi = 180^o$ through equation

$$\delta\alpha = \frac{(\delta\omega^{asym}_{\phi=0^o} + \delta\omega^{asym}_{\phi=180^o} - 2\delta\gamma)}{2} \tag{5.4}$$

6. To find parallel and perpendicular mismatch, strain, and relaxation, calculation on $d_{\parallel}$ and $d_{\perp}$ of substrate and the epilayer are needed. Equations to find $d_{\parallel}$ and $d_{\perp}$ are as follows

$$d_{\parallel} = \frac{d_{hkl}}{sin(\alpha + \delta\alpha)} \tag{5.5}$$

$$d_{\perp} = \frac{d_{hkl}}{cos(\alpha + \delta\alpha)} \tag{5.6}$$

In this work, (115) asymmetric plane is selected. d_{115} for relaxed InAs is 1.16592 and α is known to be 15.7932^o while d_{115} for substrate and epilayer is taken from RC results.

7. To calculate parallel and perpendicular mismatch, use the following equations

$$parallelmismatch = r_{\parallel} = \frac{d_{\parallel} - d_{\parallel substrate}}{d_{\parallel substrate}} \tag{5.7}$$

$$perpendicularmismatch = r_{\perp} = \frac{d_{\perp} - d_{\perp substrate}}{d_{\perp substrate}} \tag{5.8}$$

8. Strain in parallel and perpendicular direction can be calculated using the following equations

$$\varepsilon_{\parallel} = \frac{d_{\parallel} - d_{\parallel r}}{d_{\parallel r}} \tag{5.9}$$

$$\varepsilon_{\perp} = \frac{d_{\perp} - d_{\perp r}}{d_{\perp r}} \tag{5.10}$$

9. Relaxations can be calculated using the following equations

$$R_{\parallel} = \frac{d_{\parallel} - d_{\parallel substrate}}{d_{\parallel r} - d_{\parallel substrate}} x100\% \tag{5.11}$$

$$R_{\perp} = \frac{d_{\perp} - d_{\perp substrate}}{d_{\perp r} - d_{\perp substrate}} x100\% \tag{5.12}$$

The results from above RC calculations are as tabulated in table 5.3.

Table 5.3: InAs on GaAs RC calculation results

$\delta\gamma(^o)$	$\delta\alpha(^o)$	$r_{\parallel}$	$r_{\perp}$	$a_{\parallel}$(Å)
0.008395	0.006665	0.071125	0.072923	6.05568
$\varepsilon_{\parallel}$	$\varepsilon_{\perp}$	$R_{\parallel}(\%)$	$R_{\perp}(\%)$	$a_{\perp}$(Å)
-0.000411	0.001267	99.384456	101.896865	6.06577

where $a_{\parallel}$ and $a_{\perp}$ are the parallel and perpendicular lattice constants, respectively.

5.1.2.2 Calculation from RSM result

With RSM, parallel and perpendicular mismatch, strain, and relaxation of our sample can be calculated. Step by step calculations are as follows:

1. To find tilt, the same procedure can be done as in step 2 in RC calculation. However, since from RSM scan qx and qy values can be obtained, we can also use equation below to find tilt[24, 25]

$$\delta\gamma = tan^{-1}\frac{|q^{sym}_{x,\phi=0} - q^{sym}_{x,\phi=180}/2|}{(4/a_s) - |q^{sym}_{z,\phi=0} - q^{sym}_{z,\phi=180}|} \tag{5.13}$$

2. To find all properties we are looking for, firstly d spacings needed to be calculated first. In this work, calculations are based on relative measurement approach. To obtain d-spacings, use Qx and Qy values obtained from RSM. Illustrated in Figure 5.5 two RSM measurements from different planes were needed to find d spacing. The two RSM planes can be both asymmetric planes or one symmetric and one asymmetric planes. Two symmetric planes will not work because they do not contain strain information. In this work, two planes chosen were (004) and (115).

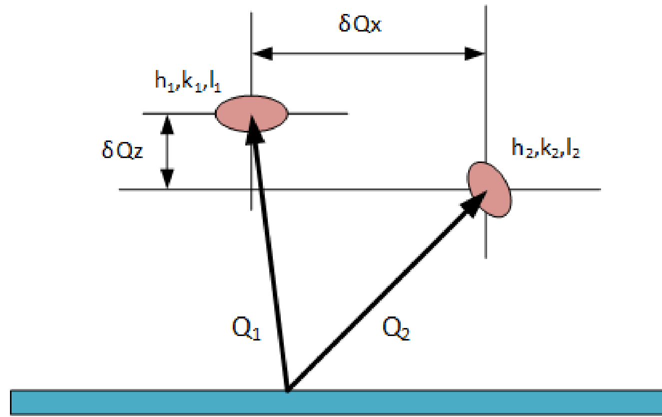

Figure 5.5: d-spacing calculation with relative measurement approach

To find $d_{\parallel}$ and $d_{\perp}$ for both substrate and layer, use the following equation:

$$d_{\parallel} = \frac{1}{\delta Qx} \tag{5.14}$$

$$d_{\perp} = \frac{1}{\delta Qy} \tag{5.15}$$

3. To calculate parallel and perpendicular mismatch, strain and relaxation, use the same equation 5.7 until 5.12.

The results from above calculations are as tabulated in table 5.3, where $\delta\gamma_{\omega}$ is tilt based on omega values using eq. 5.2 and $\delta\gamma_{q_x\&q_y}$ is tilt based on qx and qy values using eq. 5.13.

Table 5.4: InAs on GaAs RSM calculation results

$\delta\gamma_\omega(^o)$	$r_\parallel$	$r_\perp$	$\varepsilon_\parallel$	$\varepsilon_\perp$
0.005	0.071877	0.0728214	-0.000418	0.001195
$\delta\gamma_{q_x\&q_y}(^o)$	$R_\parallel(\%)$	$R_\perp(\%)$	$a_\parallel$(Å)	$a_\perp$(Å)
0.00494	98.893818	101.7334396	6.05382	6.06532

5.1.3 Discussion

Comparing the two methods, similar results on parallel and perpendicular lattice constants/mismatches and residual strain were acquired. According to the calculation the InAs later was almost 100% relaxed. This is due to the fact that 1.5 μm thick InAs layer is much thicker than the critical thickness, hence its lattice parameter relaxes back to its bulk lattice parameter. Theoretically, InAs and GaAs lattice mismatch is $\approx$ 7% in fully relaxed state[26, 27]. Our calculations shows similar results to the theory which strongly support the conclusion. From strain calculation result, strain in z direction is not equal to zero and strain in x direction is in a minus value. This suggests that the epilayer is a bit compressed in x direction and elongated in z direction. The parallel and perpendicular lattice constants of 6.05568 Å and 6.06577 Å are close to the bulk lattice parameter of 6.0582 Å. A smaller parallel lattice parameter and a bigger lattice parameter compared to the bulk value also refer to the conclusion that the thin film in an almost fully relaxed state.

Considering the simplicity of the two methods, it is much easier and faster to get the tilt using the RC method, whereas the RSM method require less effort on measurement set up (3 scans rather than 4 scans) for the measurements and easy calculation to get parallel and perpendicular lattice constant and residue strain. However, the RSM method takes much longer scanning time compared to the RC method.

The RC and RSM scan results are slightly different. This is because of the difference in resolution between RSM and RC scan. With RC, the scan step was set to be 0.01^o. While in RSM, the scan step was set to be 0.2^o. The difference in resolution lead to different values in calculation, especially on tilt as it only relies on the values of ω, while tilt value is involved until the last part of calculations. Calculation of tilt using eq.5.2 and eq. 5.13 give similar results. The slight differences are

due to rounded up numbers of omega values(only two digits after comma) because of the RSM step size of 0.02^o.

5.2 $In_xGa_{1-x}As$ layers on GaAs substrate

In this sample three layers of $In_xGa_{1-x}As$ were grown on top of a GaAs substrate in order to calibrate the In source temperatures, which correspond to different growth rates. For this sample, the Ga growth rate was fixed to be 1 μm/h and the growth time for each layer was set to be 30 minutes. . The principle for the calibration is: the Ga growth rate is calibrated by RHEED and fixed during the growth, the three $In_xGa_{1-x}As$ layers were grown with different In growth rates. The In growth rates can be calculated if the In composition can be extracted by XRD measurements. However, though the growth time for each layer is known, the layer thickness, which is determined by the total growth rates of In and Ga, is still unknown.

5.2.1 Measurement and Results

Sample was measured using HRXRD with both RC coupled scan and RSM scan methods. RC scan result is shown in Figure ref 5.6. The peak with the highest intensity corresponds to the peak from the substrate while the three smaller peaks correspond to the three $In_xGa_{1-x}As$ layers. RSM scan result can be seen as in Figure 5.8.

To calculate residual strain from RC scan, two symmetrical and two asymmetrical scans both for $\phi = 0^o$ and $\phi = 180^o$ are needed. The two symmetrical scans will be needed to find tilt, and the two asymmetrical scans are needed to find the residual strain.

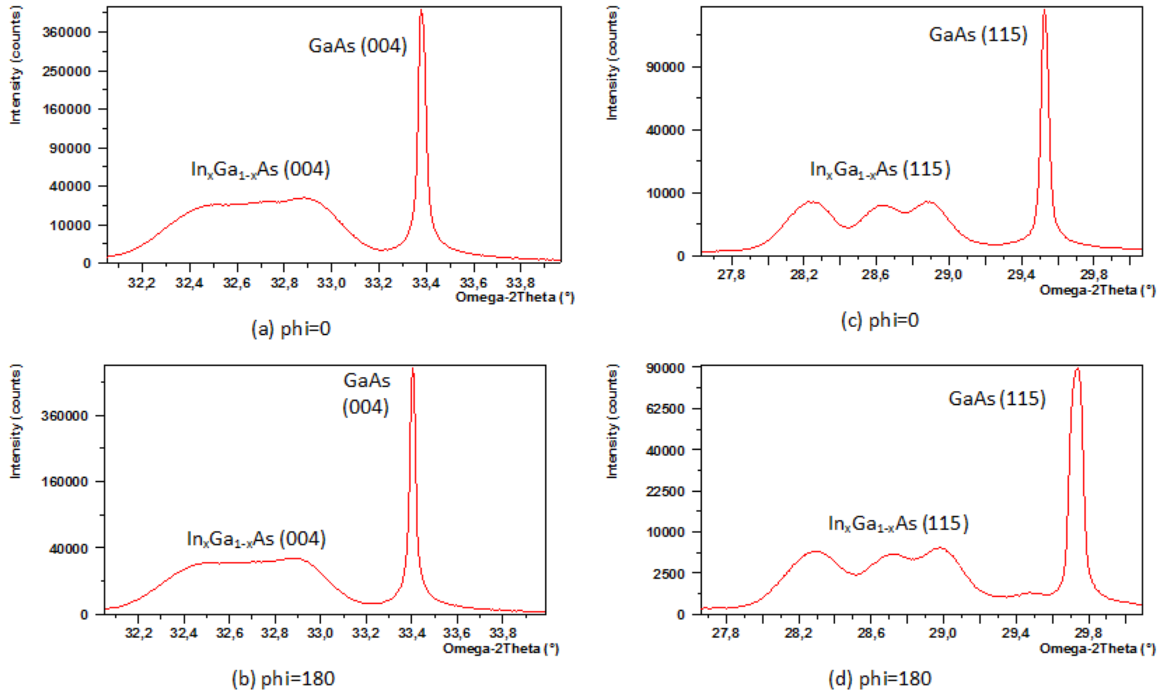

Figure 5.6: Coupled scan result of (004) and (115) plane of $In_xGa_{1-x}As$ on GaAs for $\phi = 0^o$ and $\phi = 180^o$

Table 5.5: Data of $In_xGa_{1-x}As$ on GaAs sample from RC scan result

Plane	$\phi(^o)$	Label	omega$(^o)$	2theta$(^o)$	d-spacing
(115)	0	S	29.52789	90.14478	1.087994
		L_1	28.88193	88.85287	1.100438
		L_2	28.64127	88.37154	1.105184
		L_3	28.24093	87.57086	1.113214
(115)	180	S	29.73275	90.70791	1.082699
		L_1	28.97339	89.18917	1.097158
		L_2	28.72443	88.69126	1.102025
		L_3	28.29303	87.82847	1.110612

For RSM scan, two symmetrical scans will be needed to find tilt, and one symmetrical and one asymmetrical scans are needed to find the residual strain.

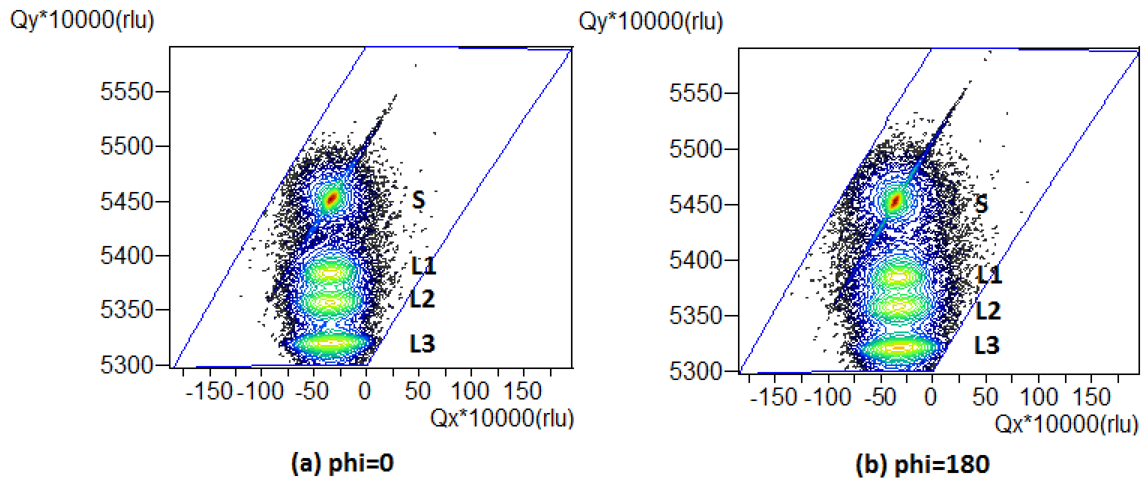

Figure 5.7: RSM(004) for $\phi = 0^o$ and $\phi = 180^o$ of $In_xGa_{1-x}As$ on GaAs

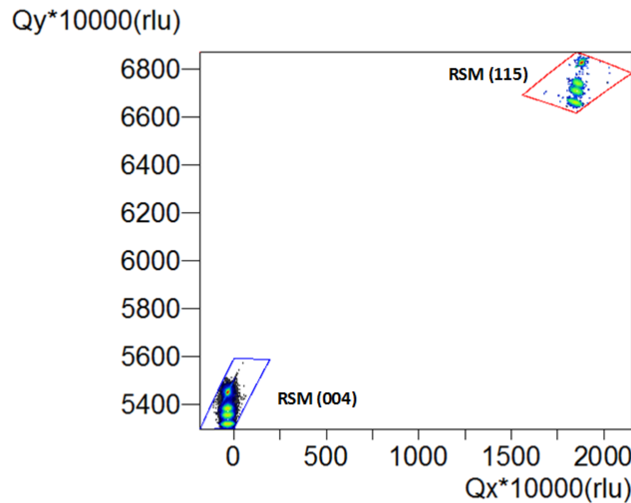

Figure 5.8: Combined graph of RSM(004) and RSM(115) of $In_xGa_{1-x}As$ on GaAs

5.2.2 Calculation method

To find the tilt, calculation from symmetric RC scans is impossible due to unclear peaks as seen in Figure 5.6. However, calculation of tilt is possible to be done using symmetric RSM scans. The same calculation can be done as discussed in the previous section. Each layer's tilt is calculated based on its tilt with respect to the substrate.

Calculation using equations as in the InAs thin film sample cannot be used for this sample as the sample's composition is unknown. To find composition of an

Table 5.6: Data of $In_xGa_{1-x}As$ on GaAs sample from RSM scan result

Plane	$\phi(^o)$	Label	omega(^{o})	2theta(^{o})	Qx(rlu)	Qy(rlu)	d-spacing
(004)	0	S	33.40000	66.07878	-0.003431	0.545205	1.412834
		L_1	32.96000	65.15310	-0.003603	0.538414	1.430650
		L_2	32.78000	64.77888	-0.003651	0.535659	1.438007
		L_3	32.52000	64.28650	-0.003498	0.532026	1.447827
(004)	180	S	33.40000	66.07878	-0.003431	0.545205	1.412834
		L_1	32.96000	65.15310	-0.003603	0.538414	1.430650
		L_2	32.78000	64.77888	-0.003651	0.535659	1.438007
		L_3	32.52000	64.28650	-0.003498	0.532026	1.447827
(115)	0	S	29.66000	90.14837	0.188189	0.682554	1.087959
		L_1	28.92500	88.75000	0.186305	0.674079	1.101448
		L_2	28.68500	88.17883	0.184820	0.670784	1.107101
		L_3	28.25000	87.45010	0.184425	0.666140	1.114440

alloy, Vegard's law as in eq.3.3 is the one to be used. However, to find x value using eq. 3.4, it is impossible to find d_R while composition is unknown. Therefore, for this sample, different approaches compared to the previous sample calculation will be used.

According to Vegard's Law, $In_xGa_{1-x}As$ lattice parameter is linearly dependent to In composition (x) provided by the following equation[28]:

$$a_{In_xGa_{1-x}As} = 6.0583 - 0.405x \tag{5.16}$$

Even though the provided d spacing from the scan can be easily converted into lattice parameter through eq. 3.1, since our sample may exhibit strain, this calculation cannot be used directly. Furthermore, the Poisson's's ratio is a function of composition and can be calculated using equation[28] below

$$poissonratio = v = 0.35 - 0.04(1 - x)) \tag{5.17}$$

where x is the In composition.

The d spacing provided by the scan is a d spacing which includes some residual strain. To find $d_\perp$ in relaxed state, introduce values of Kx, Ky, and Kz which are the ratios of the plane spacings in relaxed state in x, y, and z direction,

where

$$\frac{d_{xr}}{K_x} = \frac{d_{yr}}{K_y} = \frac{d_{zr}}{K_z} \tag{5.18}$$

and $d_\perp$ in relaxed state is defined by

$$d_{\perp r} = K_z * \frac{1-v}{1+v}(\frac{d_z}{K_z} + \frac{v}{1-v}(\frac{d_x}{K_x} + \frac{d_y}{K_y})) \tag{5.19}$$

In the calculation, it is assumed that the medium is isotropic, hence dx=dy=$d_\parallel$. Kx, Ky, and Kz are assumed to be equal to 1 because dx, dy, and dz are equal in cubic relaxed state.

Then, a calculation of composition can be done through equation

$$x = \frac{d_{\perp r} - d_{zb}}{d_{za} - d_{zb}} \tag{5.20}$$

where $d_{\perp r}$ is the relaxed d spacing in z direction, d_{za} and d_{zb} are the relaxed d spacing of InAs and GaAs, respectively. d_{za} and d_{zb} can be calculated through equation 3.1 with lattice parameter of InAs and GaAs are 6.0583 Å and 5.65325 Å, respectively. However, in equation 5.19, $d_{\perp r}$ is a function of Poisson's ratio. Since Poisson's ratio is a function of composition, the value of Poisson's ratio, composition, and $d_{\perp r}$, equation 5.17, 5.19 and 5.20 have to be done iteratively.

The results from the iterative calculations are as tabulated in table below. where x is the In composition,v is Poisson's ratio, and $d_{\perp r}$ is the relaxed d spacing.

Table 5.7: In composition, Poisson's ratio and relaxed d spacing results from iterative calculation

Scan	Label	x	v	$d_{\perp r}$
RC	L_1	0.1443	0.3158	1.0992
	L_2	0.2175	0.3187	1.1049
	L_3	0.3101	0.3224	1.1121
RSM	L_1	0.1502	0.3160	1.0997
	L_2	0.2414	0.3197	1.1068
	L_3	0.3110	0.3224	1.1122

5.2.2.1 Calculation from RC result

The difference in calculation of from RC and RSM are in the steps to obtain $r_\parallel$ and $r_\perp$ values. Steps 1 to 6 in section 5.1.2.1 can also be applied here. With the calculated

$r_{\parallel}$ and $r_{\perp}$, iterative calculation to find Poisson's ratio, composition, and $d_{\perp r}$ can be done. The parallel and perpendicular lattice constant, strain, and relaxation can be calculated as listed in section 5.1.2.1 step 7 to 9.

Table 5.8: RC calculation results of $In_xGa_{1-x}As$ on GaAs sample

Label	$r_{\parallel}$	$r_{\perp}$	$\varepsilon_{\parallel}$	$\varepsilon_{\perp}$	$R_{\parallel}(\%)$	$R_{\perp}(\%)$
L_1	0.006056	0.011872	-0.001189047	0.001126274	88.34	111.05
L_2	0.015074	0.015858	-0.000229885	0.000257037	98.49	101.68
L_3	0.022931	0.0218	-0.001870452	0.001706945	91.71	108.36

5.2.2.2 Calculation from RSM result

To get $d_{\parallel}$ and $d_{\perp}$, step 2 from section 5.1.2.2 can be used.

Tilt calculation results based on RSM results Figure 5.7 are listed in table below.

Table 5.9: Tilt calculation results from RSM

Scan type	Label	$\delta\gamma_{\omega}(^o)$	$\delta\gamma_{q_x\&q_y}(^o)$
RSM	L_1	0.3	0.262
	L_2	0.3	0.265
	L_3	0.3	0.329

To calculate residual strain from RSM scan, similar calculation steps as listed in section 5.1.2.2 step 7 to 9 were also done for this sample.

Table 5.10: RSM calculation results of $In_xGa_{1-x}As$ on GaAs sample

Label	$r_{\parallel}$	$r_{\perp}$	$\varepsilon_{\parallel}$	$\varepsilon_{\perp}$	$R\parallel(\%)$	$R\perp(\%)$
L_1	0.009014891	0.012412929	-0.001303828	0.001316723	87.25	112.33
L_2	0.016708141	0.016458834	-0.00059923	0.000543007	96.47	103.19
L_3	0.019672951	0.02412127	-0.002101812	0.002014026	90.34	109.25

5.2.3 Discussion

With RC scan, A symmetrical scan show unclear differences of epilayer peaks, while asymmetrical scan provides clear peaks. This happens because symmetrical planes with slight differences of d spacings will have slight differences of Bragg angles. Meanwhile, from asymmetrical scan, as strain is already involved here, the separation of the peaks Bragg angles are more clear. Therefore, for stacked heterostructure sample, it is best to use asymmetrical RSM scan to be able to observe clear epilayer peaks. In the calculation of strain with RC, tilt values were taken from the symmetric RSM scan. Another way to obtain tilt values using RC scan is placing the symmetrical scan (004) with (11-5) scans for $\phi = 0^o$ and $\phi = 180^o$. The difference between (115) and (11-5) planes should be enough to also see if tilt is present in the epilayer[29]. Calculation of tilt using eq.5.2 and eq. 5.13 give similar results. The slight differences are due to rounded up numbers of omega values(only two digits after comma) because of the RSM step size of 0.02^o.

In the case of $In_xGa_{1-x}As$ on GaAs substrate, a higher In composition will shift the peak more to the left. This is because the lattice constant of InAs is bigger than that of GaAs, as shown in Figure 3.4. Higher concentration of In leads to bigger lattice parameter of the alloy which decreases the diffraction angle 2theta. Results from Table 5.9 imply that the layers are tilted with respect to the substrate. There is no tilt occurs with respect to the previous layer when the layer grows on top of another.

From the calculation of relaxation, the results imply that the bottom layer of InGaAs with the smallest concentration holds the largest strain compared to the other two layers. This is most probably due to the largest lattice mismatch between the bottom layer and the substrate. The middle InGaAs layer is the least strained layer as can be seen in RSM Figure 5.9 below (compare with Figure 4.19(c)). Figure 5.9 can also be used to explain the differences in calculations between the two methods. In RSM scan, the peak chosen is the highest intensity and it is possible that not all of the peaks are in the same offset. In RC scan, the diffraction signals are collected at the same offset, hence the peak positions with regards to RSM peaks could be different. This leads to the different calculations results between the two methods.

In general, RSM needs less number of scans with two symmetrical scans

for tilt calculation and one asymmetrical scan for strain and relaxation calculation. RSM scans also have the advantage of simple and less steps in terms of calculations. RSM scan result can also be considered to be more accurate, while RC scans peaks may deviate from the real peaks. However, since RSM takes much longer time to conduct, for faster and more accurate results, two symmetric RC scans and one symmetric along with one asymmetric RSM scans is more preferable.

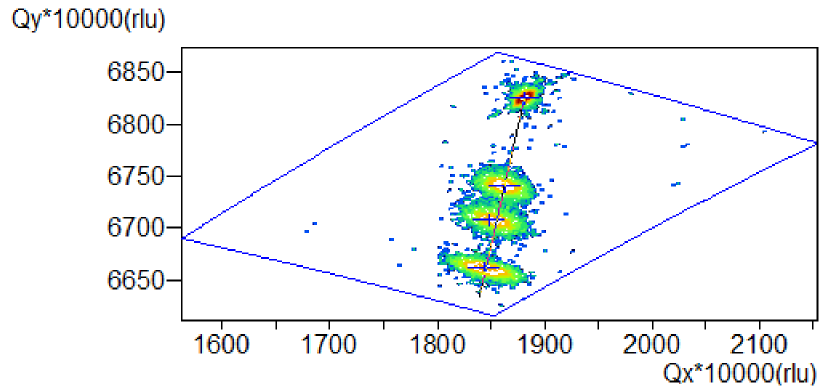

Figure 5.9: RSM (115) of $In_xGa_{1-x}As$ layers on GaAs. Second layer is more strained than the other layers.

6

XRD Measurements on Nanowire Samples

This chapter will discuss the XRD measurements on nanowire samples. Three InAs nanowire samples grown on a Si(111) were investigated. This chapter will start with a short introduction of nanowires and the growth of InAs nanowires on Si substrates. Then the XRD measurement techniques along with the results and discussions will follow.

6.1 Nanowire structure

Semiconductor nanowires represent a unique system for exploring phenomena at the nanoscale and are also expected to play a critical role in future electronic and optoelectronic devices. Among a variety of semiconductor materials, InAs nanowires have been widely investigated for high-performance nanoscale electronic device applications because of its very high room temperature (RT) electron mobility and low-resistance ohmic contacts[30]. In addition, NWs can accommodate a greater elastic strain with respect to the host substrate than is commonly seen with planar interfaces, because the free borders at the side walls allow for lateral strain relaxation [4]. Therefore attention has been attracted to grow InAs NWs on Si substrates since it may enable nanowire electronic devices seamlessly integrated with the Si platform.

Nanowires with cubic crystal structure typically grow in the (111) direction and therefore they are often epitaxially grown on (111) substrates to achieve vertically aligned nanowire growth along the surface normal[31]. However, it is widely observed that the crystallographic structure of GaAs, InAs, and some other III-V

nanowires embody occasional staking faults (SFs) originating from the presence of alternating layers of wurtzite and zincblende structure. It seems that growth of III-V nanowireson (111) substrate is strongly dominated by the hexagonal wurtzite structure, despite the fact that bulk and two-dimensional growth of these compounds leads to strictly zincblende structure. it has been found that the phase formed in the nanowires is strongly dependent on the nanowire geometry and growth parameters [add some reference].

Figure 6.1 schematically shows crystal structure of a single nanowire with pure zinc blende or pure wutzite phase that is grown on (111) oriented substrate. The difference between zinc blende phase and wurtzite phase lies on the stacking sequence of the III-V pairs layers. The III-V pair layers are usually described by A, B, and C layers as also seen in Figure 6.1[32, 33]. In zinc blende phase, there are three types of III-V pairs layers that are stacking in sequence, namely ABC sequences, while in wurtzite phase, there are only two types of III-V layers that are stacking, AB sequences. In the case of pure zinc blende nanowire, the stacking will be continuously repeated A, then B, then C, and then back to A. But in the case of mix phase of zinc blende-wurtzite phase, i.e. stacking faults, the stacking sequences may deviate, for example from zinc blende ABCABC into wurtzite ABAB.

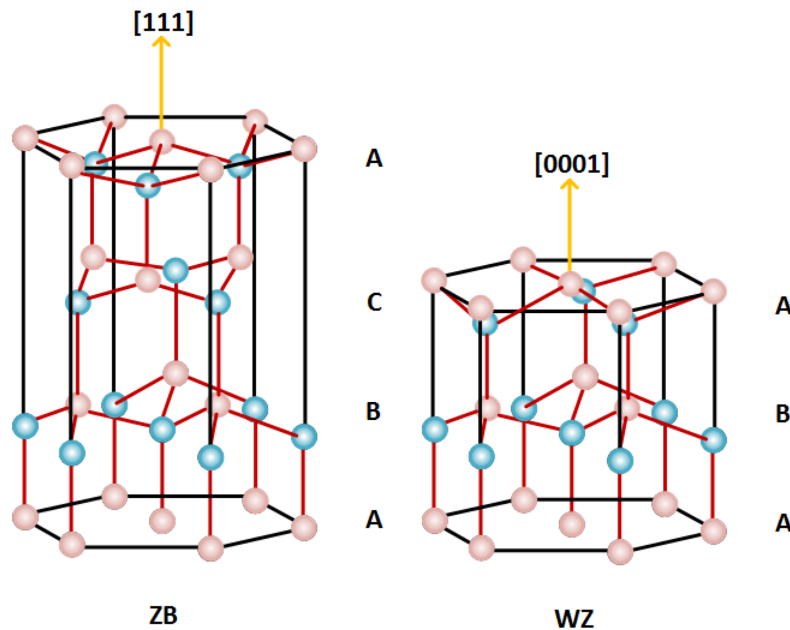

Figure 6.1: Nanowire atom structure in zinc blende and wurtzite phases grown in $<111>_c$ or $<0001>_h$ direction

There are three types of stacking faults, intrinsic (when a layer is missing), extrinsic (another layer is introduced), and twinning (a change in stacking sequence as it turns into a mirror sequence of the previous sequence. The three types of stacking faults are illustrated in Figure 6.2. Stacking faults are considered to be deleterious to carrier transport, such as ballistic transport and luminescence. Twin defect is one example in stacking fault that usually occur in nanowire which happens when a mirroring of stack happens. For example, instead of regular stack of |ABC|ABC|, it becomes |ABC|A|CBA| with a boundary layer which is illustrated by an A layer in Figure 6.2(c).

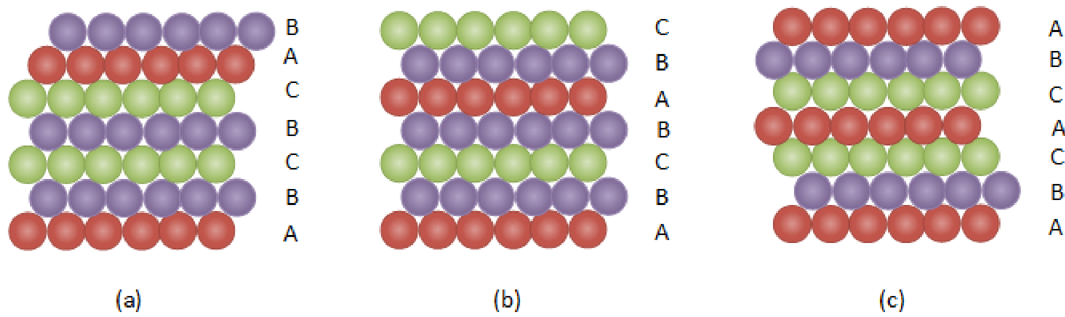

Figure 6.2: Types of stacking faults: (a) intrinsic (missing an A plane), (b) extrinsic (extra B plane) and (c) twinning (A plane as twin boundary)

6.2 Nanowire grow with MBE

Different growth techniques have been developed to fabricate NWs, such as chemical vapor deposition (CVD), molecular beam epitaxy (MBE), laser ablation, thermal evaporation, and a few other options. Most reported NW growths were governed by the vapor-liquid-solid (VLS) mechanism, either through self-induced or foreign metallic catalyst. Such processes in which the catalyst is self-assembled produce NWs that are randomly positioned and also exhibit a significant variation of diameters. A further problem with catalytic growth, mainly in the case of using gold, is that the metal catalyst will be inevitably incorporated into the NWs, which may be prohibitive for many applications. On the other hand, selective area epitaxy (SAE) on patterned substrate is essential to have a control over position, size and directionality of nanowires for homogenous and predictive performance. In the SAE approach, substrate is usually masked with patterned SiO2 layer with aperture sizes

commonly below 100 nm, and the growth conditions are appropriately chosen to restrict the epitaxial growth inside the apertures. However, current approach for nano-patterning is mainly based on e-beam lithography (EBL), which has a high cost and low throughput due to long writing times over millimeter areas. Nano-imprinting has been applied for nano-patterning to grow NWs, with a relatively lower cost and much higher throughput through a replication process. But the technique still needs EBL for stamp fabrication and innovative solutions are still needed to solve process and stamp lifetime issues for different applications .

In this work, the InAs nanowire samples being examined were grown in a catalyst-free mode using MBE on Si (111) substrates. Sample A and C were grown on colloidal lithography patterned Si substrate, and sample C was grown on substrate without lithographt patterning. This is realized by generating pinholes in the SiO2 layer with wet etching. More detail of the growth can be found in Ref. [1].

Scanning Electron Microscopy or SEM was done to get an image of the morphology of the nanowires. Knowledge on the nanowire environments, including the density and the presence of cluster are needed for further discussion on the tendency of forming phase in nanowires. The tendency of phase formed in nanowire is also affected by the diameter and length [34]. Figure 6.3 shows SEM result gathered. The density, diameter and length of sample A, B, and C based on the SEM results are tabulated in table 6.1. This data was gathered using ruler tool of ImageJ. From the top, nanowires grown on Si<111> exhibit hexagonal geometry[35]. This is due to the growth direction of (111)ZB which leads to six sidewall facets that correspond to the {110} family of orientations[36]. Clusters also present in a large amount on sample A and B, while in sample C there is only a few of clusters.

Table 6.1: Nanowire samples data

Sample	Diameter (nm)	Length (nm)	Cluster	Density
A	67±5	601±10	yes	high
B	111±5	596±10	yes	high
C	194±5	177±10	no	low

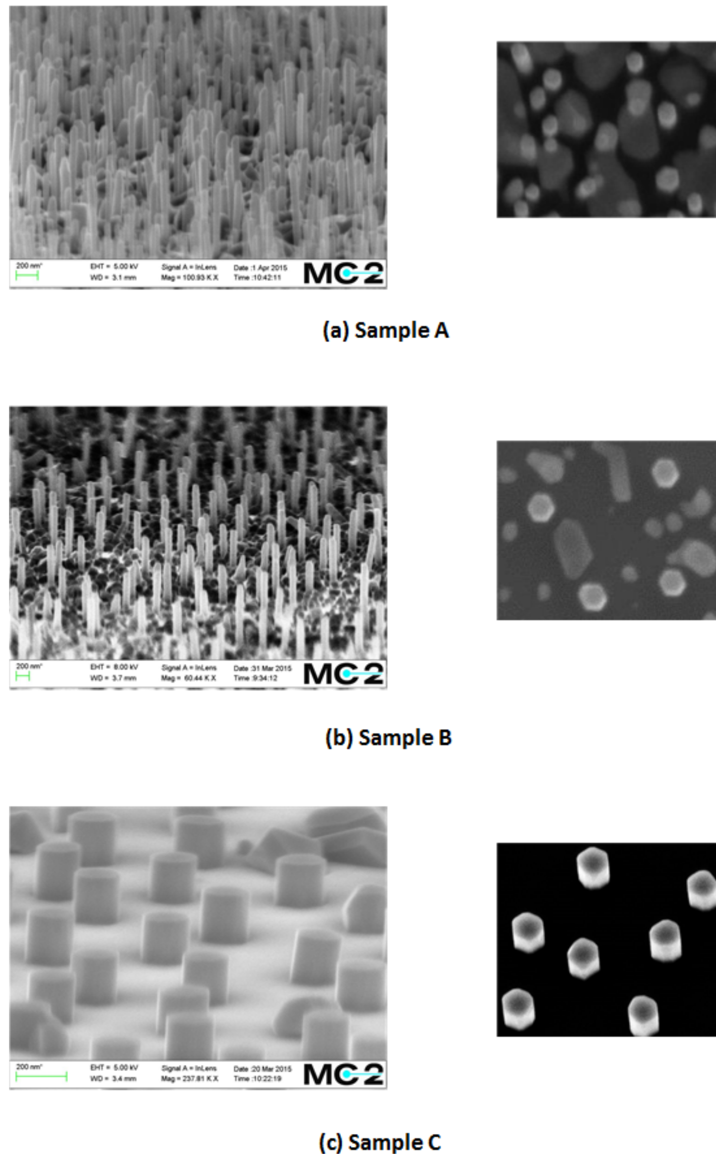

Figure 6.3: Sample A, B, and C as seen using SEM. Left figures are the side view (75° tilt) and right figures are the top view (except samples C is 30° tilt). Top view shows hexagonal geometry of grown nanowires.

6.3 Nanowire Characterization

To characterize nanowires using XRD, people have been using different types of XRD measurement, including out of plane, GIXRD, and in plane. In this work, the use of different configurations and different measurement types will be thoroughly discussed.

6.3.1 HRXRD configuration

The use of out of plane RC coupled scan measurement for nanowire samples has been usually used to identify nanowire phase and other properties such as strain, etc.

According to [35], the existence of both phases of nanowires can be detected using out of plane RC coupled scan measurement as the peaks from wurtzite phase will be in a different Bragg angle than peaks from zinc blende phase. However, through some measurements during this work, the use of only RC coupled scan is considered to be not adequate to obtain results that are necessary for further analysis.

Coupled scan 2theta-omega results for all three samples are presented in Figure 6.4. The diffraction plane was set to be (331). For all the measurements the step size was set to be 0.02^o. 2theta-omega scan results of sample A and C both show clear and visible peak of InAs nanowire (331)ZB, meaning there is nanowire with zinc blende phase present in sample A and C. Though, the existence of (105) wurtzite peak that is expected to be present at a Bragg angle of 71.85^o did not appear at both graphs. A conclusion whether the nanowires in sample A and C are pure zinc blende or a mixed phase of ZB/WZ, cannot be yet to be drawn based only on these graphs. Smaller intensity of nanowire peak for sample C is due to the short nanowires grown and also due to the less dense nanowires, resulting in a lower intensity contribution from nanowire planes. While in sample B, no clear zinc blende nanowire peak was observed. To see peaks with different offsets, RSM scan had to be conducted.

RSM scan results are shown in Figure 6.5. Peaks of (331)ZB, (105)WZ, and (422)ZB were observed in sample A and C, indicating mixed ZB/WZ phase nanowires grown on top of the substrates. All these three peaks appears to be in the same Qx but different Qy. The appearance of (422) at the same azimuth with (331) implies an existence of twin defect within the nanowire[37]. Essentially, sets of planes {422} and {331} are related to each other by 60°, meaning that a change of azimuth of 60° will get us from one set of planes {331} into {422}. Since the periodicity of a zinc blende is 120°, when a twin defect exists, the reflections will repeat with periodicity of 60°. This leads to 60° difference as well as periodicity for both (422) and (331). Therefore, both reflections of (422) and (331) will appear

every 60° of azimuth. Meanwhile, sample B shows only (105)WZ peak indicating rich wurtzite phase for sample B.

For better analysis and clear peaks from nanowire planes, the graphs presented in Figure 6.5 are all plotted in an azimuth where substrate peak is not present. An out of plane measurement shines the sample with high energy causing it to penetrate deep into the substrate. This leads to a high intensity of substrate peak. Nanowire sample is typically 200-1000 nm tall and the density is varied, while the substrate is typically 360 μm thick. Consequently, the peak intensity from substrate will dominate while the contribution from nanowire is small. Shown in Figure 6.6(a) is RSM of sample A after an alignment based on the substrate peak. Substrate peak dominates while peaks from nanowire can barely be seen. To solve this, a selection of azimuth come into play. Substrate is Si (111)ZB with peak periodicity of 120° while nanowire ZB peak has a periodicity of 60°. By choosing an azimuth where the substrate peak does not appear, a strong and better intensity of nanowire peak can be obtained as shown in Figure 6.6(b) for sample B.

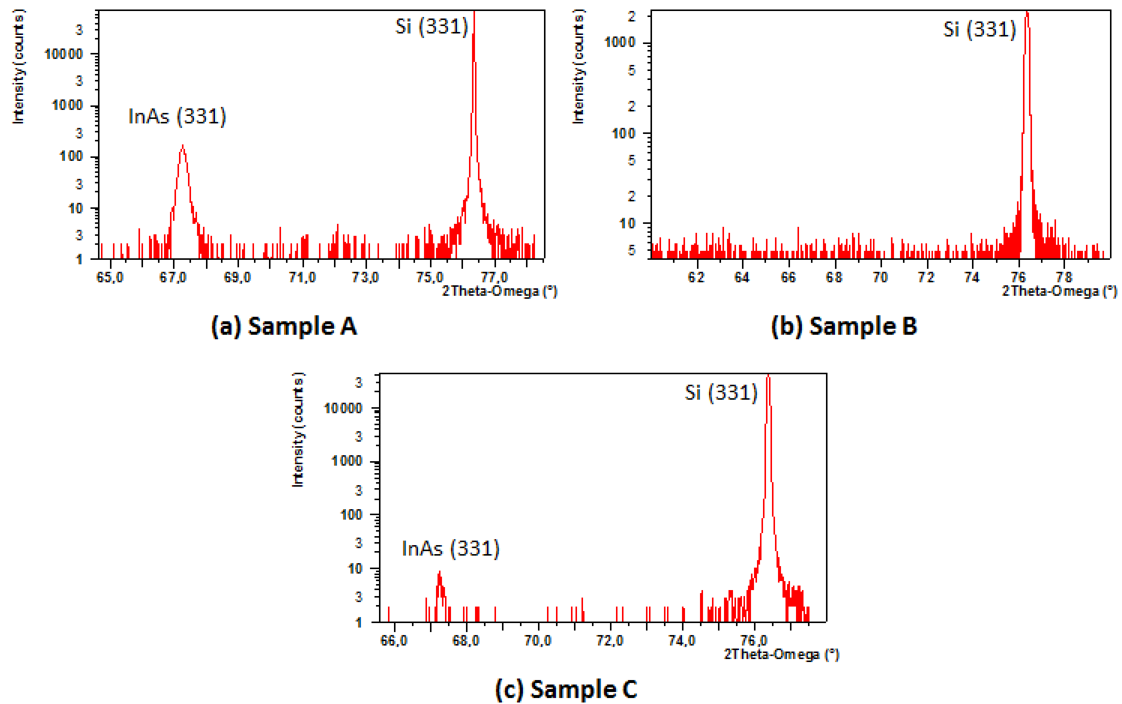

Figure 6.4: (331) coupled scan of sample A, B, and C

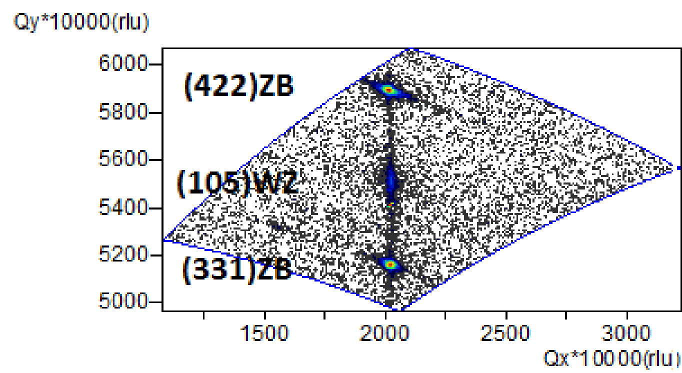

(a) Sample A

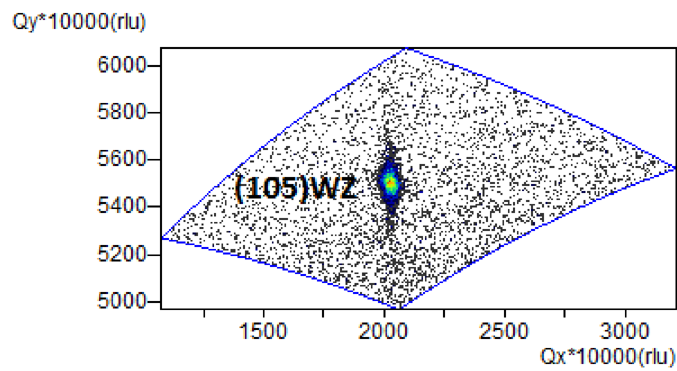

(b) Sample B

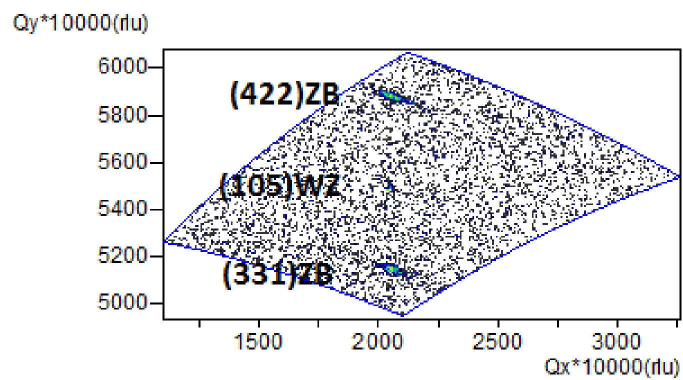

(c) Sample C

Figure 6.5: a) and (c) RSM scan results of sample A and C show (105)WZ, (422)ZB, and (331)ZB peaks at the same Qx. (b) RSM scan result of sample B indicates a presence of wurtzite rich phase nanowires

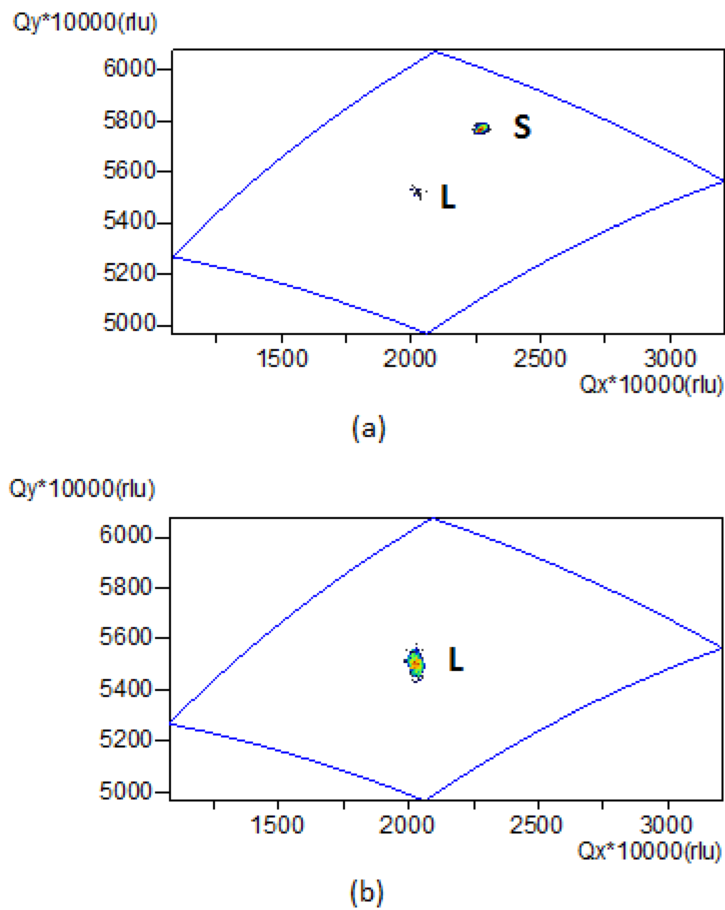

Figure 6.6: (a) Sample B RSM with substrate peak. Peak intensity is dominated by substrate's peak. (b) Nanowire peak is presented clearly after carefully aligning

6.3.2 X-ray lens configuration

X-ray lens configuration can be used for phase identification. It can be used for out of plane and in plane measurement. In this thesis lens measurement was used in both type of measurements.

6.3.2.1 Out of plane X-ray lens measurement

In this measurement, the source is set in point focus and parallel plate collimator was used as diffracted beam optic. All alignment procedures conducted was similar to the standard alignment out of plane procedures. A manual beam attenuator of

Cu 0.3 micrometer was used in order to prevent direct beam from source to detector.

With out of plane configuration, the penetration depth is deeper, hence the contribution from subtrate's planes is dominating. As seen in Figure 6.7 the peaks observed with (422) coupled scan are all dominated by substrate peaks, while the peak from (422) ZB is embedded together with the peak from substrate at Bragg angle of $\approx 77^o$. This can be proven by doing a phi scan at $2\theta = 77^o$ which shows peak periodicity of 60° instead of 120°, indicating that there are intensities from diffraction planes of nanowires. Numbers of substrate planes can be detected by this configuration, unlike HRXRD. This is due to the use of different optics between the configurations. Since X-ray lens configuration uses a parallel plate collimator and a proportional detector with no anti scatter part, all scattered intensities are detected. While HRXRD is equipped with Pixcel 3D detector with an anti scatter, eliminating the background scattered intensities.

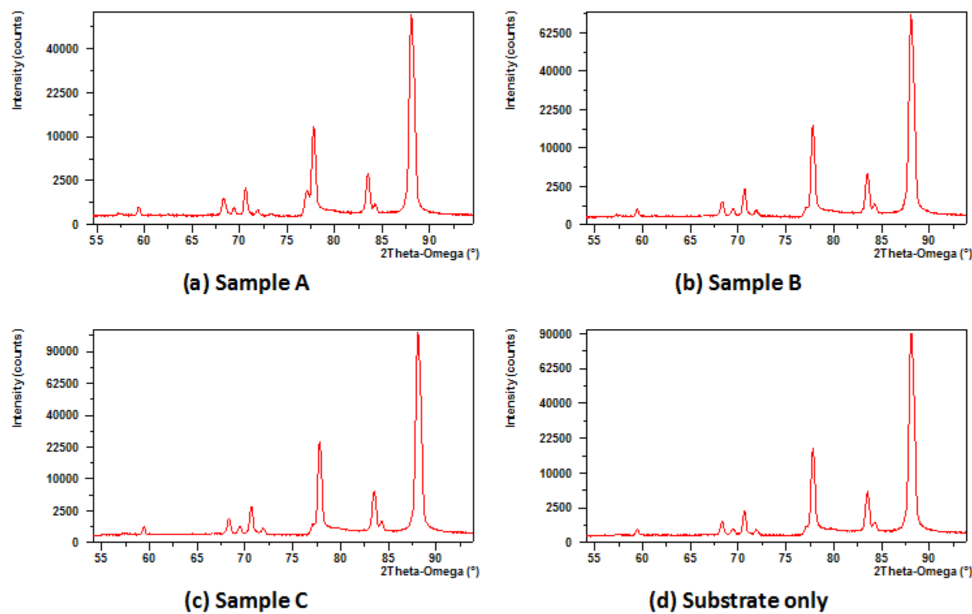

Figure 6.7: (a), (b), and (c) Coupled scan results for sample A, B, and C using X-ray lens measurement respectively. (d) shows coupled scan result from the substrate. The peaks are totally dominated by substrate's peaks

To obtain a clear sign of nanowire peaks, RSM is a better solution. With RSM, the peaks contributed from planes with similar in plane lattice constant can be distinguished with one measurement as seen in Figure 6.8. The alignment was done for (422) plane. (422)ZB, (105)WZ, and (331)ZB peaks appears in the graph for

sample A and C, while in sample B, only (105)WZ that can be observed. This result agrees with the previous HRXRD RSM result. From this result, a conclusion can be drawn that sample A and C is a mix of zinc blende and wurtzite while sample B composed of rich wurtzite phase. RSM measurement with lens configuration provides all peaks necessary for analysis where the straight red lines are the peaks from substrates. A use of grazing incidence to limit the penetration depth using this method might provide a better result as the intensity from the substrate would not be as strong.

Beam from an X-ray lens is spread in two dimension in a circular shape with a diameter that is dependent on the width of the opening slit. The diameter of the beam coming out of X-ray lens is 7 mm. This point focus-X-ray lens combination enables us to characterize a larger area of the sample compared to line focus-monochromator combination. The disadvantage of this combination lies on the resolution. This type of combination leads to a lower resolution result. A larger area of illumination accounts for a wider spread of microscopic tilts and finite grain sizes, leading to a bigger FWHM of the peaks compared to the HRXRD results. Table 6.2 listed comparisons of the FWHM in Qx and Qy of all three samples.

6.3.2.2 In plane X-ray lensmeasurement

Measurement with in plane X-ray lens configuration uses exactly the same optics used in the out of plane X-ray lens measurement. What differs is the goniometer positions which was rotated 90 degrees and chi was on 90 degrees as shown in Figure 4.13. With in plane configuration, the diffraction planes are the ones that perpendicular to the surface of symmetric planes. These measurement was carried out with the aim to eliminate the contribution of the silicon substrate.

In plane measurement technique is one technique that has been commonly used in nanowire characterization XRD, especially in the case of less dense and short nanowires as the contribution intensity from substrate will dominate almost fully, making it hard to see the peak from the grown nanowires. Therefore, in plane measurement in which penetration depth is limited to 100 nm, had been chosen in phase analysis XRD measurement. In plane scan result is shown in Figure 6.9.

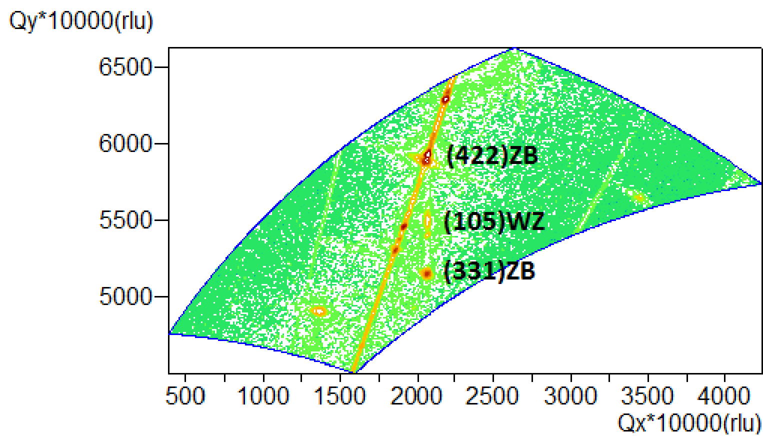

(a) Sample A

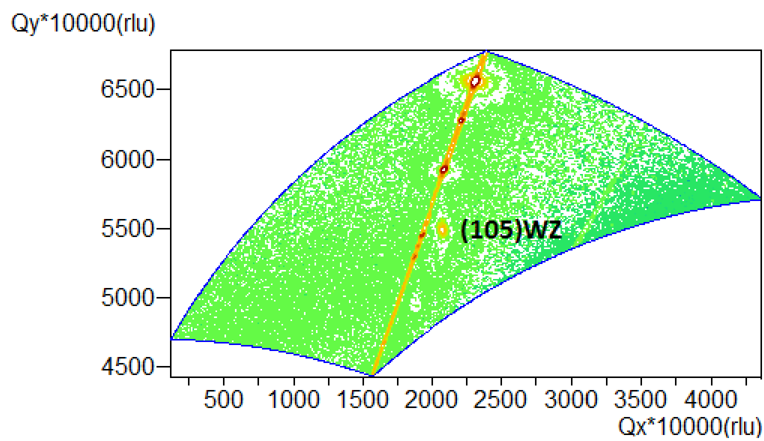

(b) Sample B

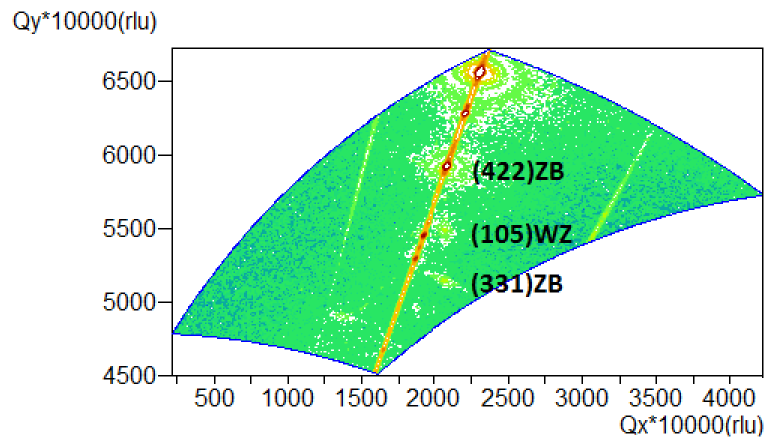

(c) Sample C

Figure 6.8: (a), (b), and (c) RSM scan results using X-ray lens measurement. (422)ZB, (105)WZ, and (331)ZB peaks appear in the graph for sample A and C, while only (105)WZ appears in the graph for sample B.

Table 6.2: FWHM comparisons of X-ray lens and HRXRD RSM results

Sample	Configuration	Plane	FWHMx	FWHMy
A	X-ray lens	(422)ZB	0.003378	0.006782
		(105)WZ	0.003308	0.008634
		(331)ZB	0.003124	0.003260
	HRXRD	(422)ZB	0.002227	0.001290
		(105)WZ	0.001623	0.002640
		(331)ZB	0.002203	0.001603
B	X-ray lens	(105)WZ	0.0074851	0.0062954
	HRXRD	(105)WZ	0.003324	0.004799
C	X-ray lens	(422)ZB	0.0049440	0.0019316
		(105)WZ	0.0046001	0.0046148
		(331)ZB	0.0046237	0.0063084
	HRXRD	(422)ZB	0.001162	0.000317
		(105)WZ	0.000639	0.000290
		(331)ZB	0.000765	0.000400

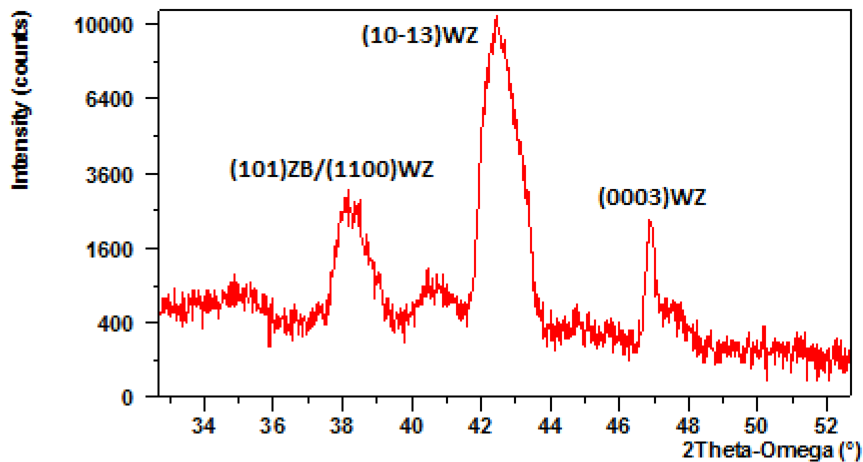

Figure 6.9: In plane measurement result on sample B

Unfortunately, due to some technical issues during this measurement, only sample B was measured using in plane measurement method. In plane measurement uses X-Ray lens as incident beam optic and parallel plate collimator as the diffracted beam optic. Sample B average length is 500 nm. Measurement with grazing incidence in plane penetration depth is only up to 100 nm which means that only the top of the nanowire will be measured. The alignment was chosen for the peak at Bragg

angle of wurtzite nanowire. The three peaks corresponds for (101)ZB/(1100)WZ, (10-13)WZ, and (0003)WZ plane. (101)ZB and (1100)WZ are symmetrical planes in perpendicular direction for both zinc blende and wurtzite structure. The intensity from both planes are in similar Bragg 2θ angle. However, it is possible that the appeared intensity came only from wurtzite structure. This result is a supporting evidence of wurtzite structure existence in nanowires of sample B.

6.4 Transmission electron microscopy (TEM)

Characterization of nanowire atomic structure is usually done by TEM. TEM provides the structural information in atomic scale, which is usually used to characterize the crystalline phase in nanowires. However, TEM usually need complex sample preparation and the instrument is more expensive. Here, our target is to find a reliable connection between the TEM and XRD measurement. And use cheap and fast XRD measurements to guide the growth in the future.

Transmission Electron Microscopy abbreviated as TEM uses electron transmission to characterize and get an image of the structure of a material. In TEM, the radiation is focused onto the sample using electromagnetic field created by current which directly control the focus. A fluorescence plate is used in TEM as the imaging device. As electrons cannot be seen with naked eye, the fluorescence plate helps to provide visibility as it will fluorescent when an electron hit the surface.

Electron can be treated as a wave that interacts and scatters when it is in contact with a crystal. The scattering image in real space can be also transformed as a diffraction pattern when the back vocal plane is measured. This diffraction pattern corresponds to the reciprocal lattice projection. The diffraction pattern of pure ZB, pure WZ, and mix of ZB/WZ differs in terms of the possible zone axis and facets.

Figure 6.10 shows TEM image of sample A and B along with their corresponding diffraction pattern. Unfortunately, a good clear image of crystal structure using TEM for sample C was unsuccessful due to the large diameter of the nanowires. The lowest zone axis of each diffraction pattern can be calculated and compared to an existing table adapted from [2] to draw a conclusion. The right side of Figure 6.10

shows the calculated three closest diffraction spots from the center and intermediate angles of each sample. This method was also conducted by [2]. The calculation results are tabulated in table 6.3. By comparing the results with calculation results adapted from [2], calculation results based on TEM image for sample A and B shows a tendency to a conclusion that sample A has a mix ZB/WZ phase while sample B has a rich wurtzite structure. These results support XRD measurements results conducted in this work. The alternating dark and bright parts in the TEM images indicates the existence of twin defects.

Another way to figure out the structure of a nanowire of a TEM result is by observing the arrangement of atoms. Figure 6.11 shows the difference in the arrangement of atoms for different type of misalignment and phase in nanowires seen with TEM [38]. Unfortunately, our TEM results were not high resolution enough to be able to identify the structure with defects. Although, it can be seen that some stacking faults can be seen in some nanowires of sample B, but the amount can be considered as really small. This might be the reason of why there were no InAs ZB peaks presents in all XRD measurements for sample B.

Table 6.3: (Top) Calculation results adapted from [2], and (bottom) calculation results based on TEM results for sample A and B

Structure	R1/R2	R2/R3	R1/R3	$\phi_{12}(^o)$	$\phi_{23}(^o)$	$\phi_{13}(^o)$
Wurtzite	0.94	0.94	0.88	90	27.94	62.1
Mix ZB/WZ	0.61	0.85	0.52	90	31.48	58.52
Zinc blende	1	0.87	0.87	70.53	54.74	54.74
Sample	**R1/R2**	**R2/R3**	**R1/R3**	$\phi_{12}(^o)$	$\phi_{23}(^o)$	$\phi_{13}(^o)$
A	0.58	0.95	0.545	98.5	32.159	59.261
B	0.9403	0.934	0.879	90.468	28.032	61.834

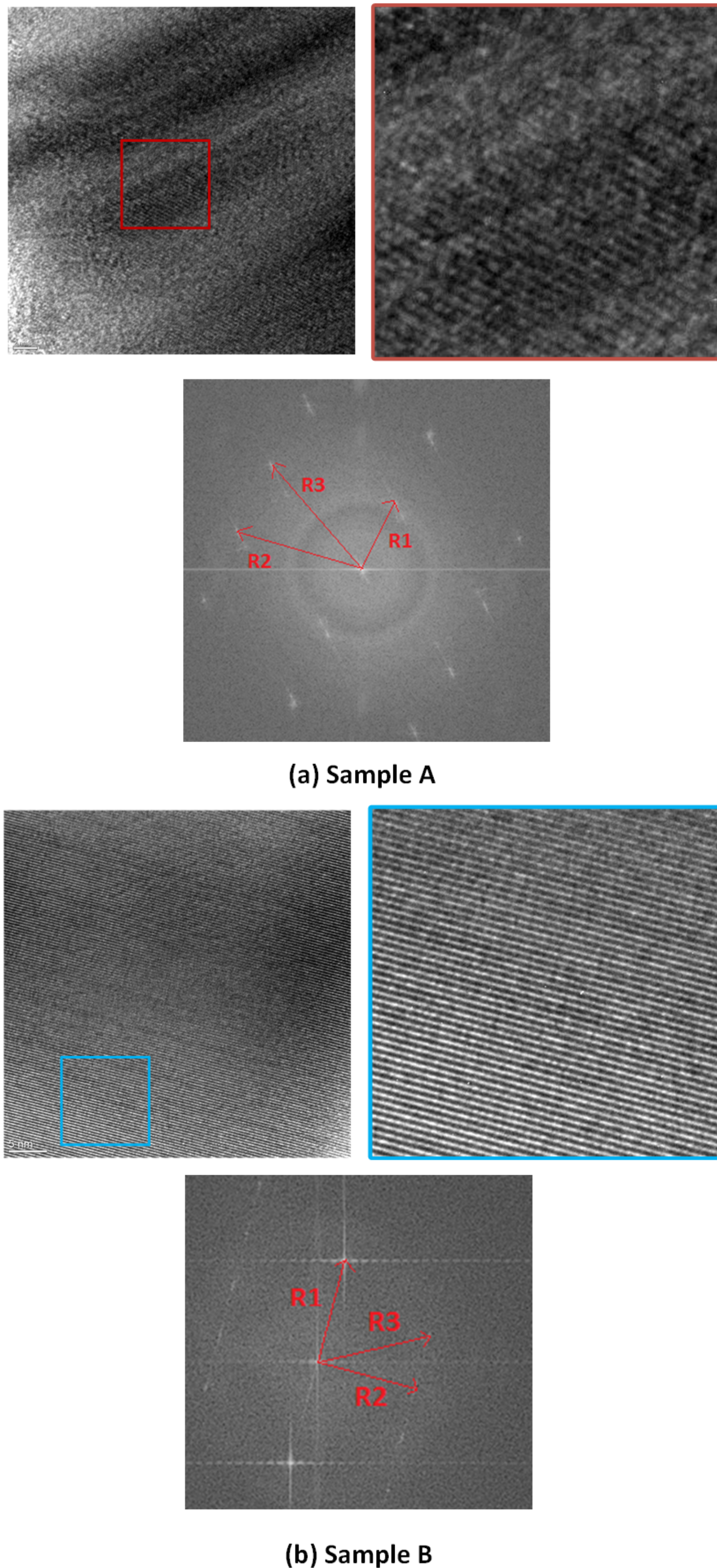

Figure 6.10: TEM results and calculated diffraction spots for sample A and B. Left pictures are the actual TEM images, right pictures are the zoom in of the images, and bottom images are the FFT results of the images.

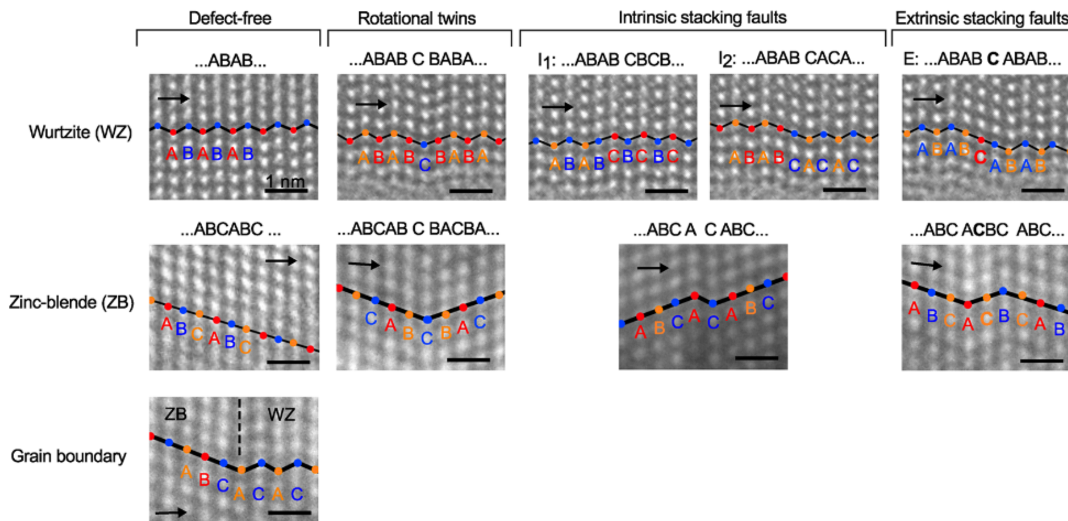

Figure 6.11: TEM images observation showing defect free, rotational twins, and intrinsic and extrinsic stacking faults in InAs and $InAs_{1-x}Sb_x$ nanowires [38]

6.5 Discussion

Through some calculations, the relaxation state of the three nanowires reach almost 100%, meaning the nanowires are in almost fully relaxed state. In thin films, defects usually formed due to strain that is released in a lattice mismatched substrate-grown layers. The defects may cause a harmful effect to the overall device performance. Nanowire, in this matter, opens the possibility of relaxed structure that is free defects because the edges of the nanowires are able to expand or compress and release the strain. Other studies show that the strain release of nanowires with highly mismatch materials already happened at early stage of nanowire growth[37, 39]. Defects caused by release of strain might present but only at the interface between substrate and nanowires. The strain release from the nanowires sidewalls enables us to form heterostructures material using high lattice mismatch materials. However, the free standing nanowires is still prone to stacking faults as can also be seen with TEM in Figure 6.10 and also proven by XRD scan when two zinc blende peaks appear at the same azimuth.

Phases formed in grown nanowires are influenced by growing time (diameters), the material source fluxes (composition of the alloy), also by the grow temperature. Studies on InAs nanowire phases, both with modeling and experimentally

have been carried out by researchers. Diameter and length of the grown nanowires also shoen to have some influences in the formation of the phases. One paper had done modeling for InAs nanowire phase, where the results showed that the nanowire with a diameter of less than 5 nm are more likely to have a wurtzite phase because the energy required for the reconstruction of the surface, is smaller. While for nanowire with a diameter above 5 nm, most likely will be a zinc blende phase. For a nanowire with a size of 10 nm, the possibility for the formation of a mixture between zinc blende and wurtzite will be high because the free energy of wurtzite and zinc blende will be similar[34]. It is also disclosed by another researcher, that the general trend for the nanowire phase is dominant wurtzite to a thin wire and dominant zinc blende for thick wire. Nevertheless, everything is still dependent on the growing condition of the nanowires, for example zinc blende phase is likely formed in thinner nanowire if a higher temperature is used[40]. Another paper revealed the effect of growth temperature on phase formation of nanowires where zinc blende phase will dominate for NWs grown at low temperatures and wurtzite phase accompanied by SFs and zinc blende segment dominate at high growth temperatures. These results obtained from the nanowire diameter of 55 nm with a length 3 micrometer [41]. In this work, however, the formed phase did not follow the trend of the modelling results. This could happen due to the different temperature and environment during growth.

Each measurement technique has its own advantages and disadvantages over the other. In terms of measurement time, table C.1 in Appendix C lists all measurement time for each measurement as a comparison. Measurements using X-ray lens can be considered to be easier in terms of sample alignment and it also gathers all the scattered intensities, hence better resolution of nanowire peaks. However, the amount of time needed to conduct one RSM scan using X-ray lens configuration is much longer as the scan range is wider. Also, using parallel plate collimator and separate proportional detector, the advantage of using scanning line mode that can only be conducted using Pixcel 3D detector which could measure 255 point at one step cannot be applied, leading to a much longer scanning time. In terms of coupled scan, both with HRXRD and X-ray lens coupled scans had been proven to be not adequate to obtain necessary data. Hence, RSM is necessary to be done. In plane measurement using coupled scan result turned to be a prove of the existence of wurtzite phase for sample B.

Lattice parameter calculation was conducted using equation 3.2. Obtained calculation results are tabulated in table 6.4. According to the theory, ideal c/a value ZB is 1.633 Å[42]. The ratio of c/a results on sample A and C is larger than the ideal value due to the mixed ZB/WZ phase. Lattice parameter is a function of WZ and ZB composition within the nanowire. Nanowires with zinc blende structure exhibits smaller lattice plane spacing in [111] direction, hence the embedded wurtzite structure in the nanowire leads to a larger c/a value. Similar results were also obtained by [42] and [43] where c/a ratios were larger than ideal ZB 1.633 Å value when wurtzite phase is composed within the nanowires. Meanwhile, wurtzite structure nanowires c/a ideal value is theoritically $\approx$ 1.642 Å [44]. A calculation result reported by [45] showed an ideal wurtzite c/a value of 1.645 Å. However, our sample B result is larger than both references. This is possibly caused by strain in in-plane direction, leading to a smaller value of a and larger value of c, hence a bigger value of c/a.

Table 6.4: Lattice parameter in zinc blende and wurtzite calculation for sample A, B and C

Sample	a(Å)	c(Å)	c/a
A	4.285	6.9803	1.6383
B	4.252	7.0332	1.6541
C	4.278	6.9895	1.6338

7

Conclusion

This work had presented the use of XRD to find material properties such as tilt, mismatch, lattice constant, residual strain, and phase determination of semiconductor materials. XRD characterization technique had been proven to be a simple, effective, and efficient to characterize heterostructure thin films and nanowires samples.

XRD measurements results using HRXRD with out of plane for both RC and RSM scans on thin film and compositionally graded stacked heterostructure samples had been presented. Calculations on sample properties, including tilt, parallel and perpendicular mismatch, parallel and perpendicular lattice constant, and residual strain and relaxation, based on acquired RC and RSM XRD scans had been listed and results had been discussed. Obtained results from RC and RSM scans led to similar results with slight differences in numbers due to difference in scan resolution. RSM scans were proven to be more efficient in terms of calculations but it requires longer time to conduct. For efficient measurement, two symmetrical RC scans with phi=0° and phi=180° for tilt calculation and one symmetric along with one asymmetric RSM scans for strain and relaxation calculation is prefered.

Phase determination of nanowire samples had been conducted using HRXRD and X-ray lens configurations in out of plane and in plane measurements for both RC and RSM scans. The differences in configurations, measurements, and scans results had been presented, compared, and discussed. For nanowire samples, it is strongly suggested to do RSM scans instead of RC scans both with HRXRD and X-ray lens configuration, to obtain more thorough results. Measurement with X-ray lens takes longer time but gathers all intensities and therefore is more preferable. The results on nanowire samples had been supported by TEM results. The acquired results were proven to be similar to what had been analyzed from TEM images.

Some practical and calculation issues still need to be addressed. All calculations done in this work had been done manually following the equations provided. More thorough simulations using the software would be needed for comparison. Some trials on the software in regards to find the sample properties also need to be explored further. In terms of characterization techniques, additional work especially on in plane measurements with RSM scan still need to be further investigated. XRR measurement also need to be explored to be able to find other properties such as the thickness and surface roughness of the samples.

References

[1] Elham Fadaly. *Molecular Beam Epitaxy of Catalyst-Free InAs Nanowires on Si (111)*. Master thesis, Chalmers Institute of Technology, 2015.

[2] Nino Leander Bartolo Ziino. *Transmission Electron Microscopy on InAs Nanowires*. University of Copenhagen, 2011.

[3] Shumin Wang. *Lattice Engineering: Technology and Applications*. CRC Press, 2012.

[4] Magnus W Larsson, Jakob B Wagner, Mathias Wallin, Paul Håkansson, Linus E Fröberg, Lars Samuelson, and L Reine Wallenberg. Strain mapping in free-standing heterostructured wurtzite inas/inp nanowires. *Nanotechnology*, 18(1):015504, 2007.

[5] Sharon Ann Holgate. *Understanding Solid State Physics*. CRC Press, 2009.

[6] William Lawrence Bragg. The diffraction of short electromagnetic waves by a crystal. *Proceedings of the Cambridge Philosophical Society*, 17(43):4, 1913.

[7] Philip Hofmann. *Solid State Physics: An Introduction*. John Wiley & Sons, 2015.

[8] Neil W Ashcroft and N David Mermin. *Solid State Physics*. Saunders, Philadelphia, 1976.

[9] Peter Luger. *Modern X-ray Analysis on Single Crystals: A Practical Guide*. Walter de Gruyter, 2014.

[10] Hector Cotal, Chris Fetzer, Joseph Boisvert, Geoffrey Kinsey, Richard King, Peter Hebert, Hojun Yoon, and Nasser Karam. Iii–v multijunction solar cells

for concentrating photovoltaics. *Energy & Environmental Science*, 2(2):174–192, 2009.

[11] Charles Kittel. *Introduction to Solid State Physics*. John Wiley & Sons, Inc, 2005.

[12] Calculation of strain. *XRD application note PANalytical*, 2014.

[13] Yvon Cordier, Sylvain Bollaert, Mohammed Zaknoune, Jean Dipersio, and Denise Ferre. Inalas/ingaas metamorphic high electron mobility transistors on gaas substrate: influence of indium content on material properties and device performance. *Japanese Journal of Applied Physics*, 38(2S):1164, 1999.

[14] WE Hoke, PJ Lemonias, JJ Mosca, PS Lyman, A Torabi, PF Marsh, RA McTaggart, SM Lardizabal, and K Hetzler. Molecular beam epitaxial growth and device performance of metamorphic high electron mobility transistor structures fabricated on gaas substrates. *Journal of Vacuum Science & Technology B*, 17(3):1131–1135, 1999.

[15] Sadao Adachi. *Physical Properties of III-V Semiconductor Compounds*. John Wiley & Sons, New York, NY(USA), 1992.

[16] M Schuster, PO Gervais, B Jobst, W Hösler, R Averbeck, H Riechert, A Iberl, and R Stömmer. Determination of the chemical composition of distorted ingan/gan heterostructures from x-ray diffraction data. *Journal of Physics D: Applied Physics*, 32(10A):A56, 1999.

[17] Walter S Knodle and Robert Chow. *Handbook of Thin Film Deposition Processes and Techniques. Molecular Beam Epitaxy: Equipment and Practice*. William Andrew, 2001.

[18] Paul F Fewster. *X-ray Scattering from Semiconductors*. World Scientific, 2003.

[19] Toru Mitsunaga. X-ray thin film measurement techniques ii out of plane diffraction measurements. *Rigaku journal*, 25(1), 2009.

[20] In plane diffraction. *XRD application note PANalytical*, 2014.

[21] Shintaro Kobayashi. X-ray thin film measurement techniques iv. in plane xrd measurement. *The Rigaku Journal*, 26(1), 2010.

[22] Miho Yasaka. X-ray thin film measurement techniques v x-ray reflectivity measurement. *Rigaku journal*, 26(2), 2010.

[23] Huan Zhao, Alexandra Malko, and ZH Lai. Effect of bismuth on structural and electrical properties of inas films grown on gaas substrates by mbe. *Journal of Crystal Growth*, 425:89–93, 2015.

[24] Wan Khai Loke, Kian Hua Tan, Satrio Wicaksono, Soon Fatt Yoon, Man Hon Samuel Owen, and Yee-Chia Yeo. Effect of growth temperature on the epitaxy strain relaxation and the tilt of inxal1- x as graded layer grown by solid-source molecular beam epitaxy. *Journal of Physics D: Applied Physics*, 45(50):505106, 2012.

[25] D Lee, MS Park, Z Tang, H Luo, R Beresford, and CR Wie. Characterization of metamorphic inxal1- xas/ gaas buffer layers using reciprocal space mapping. *Journal of applied physics*, 101(6):063523, 2007.

[26] Marius Grundmann, Oliver Stier, and Dieter Bimberg. Inas/gaas pyramidal quantum dots: Strain distribution, optical phonons, and electronic structure. *Physical Review B*, 52(16):11969, 1995.

[27] Craig Pryor. Eight-band calculations of strained inas/gaas quantum dots compared with one, four, and six-band approximations. *Physical Review B*, 57:7190, 1998.

[28] Ioffe Physico technical Institute Electronic Archive. Electronic archive new semiconductor material characteristic and properties: Gaxin1-xas, 2001.

[29] Qinfen Gu. *Characterization of GaAs-based Long Wavelength Laser Materials by X-Ray Diffraction.* Master thesis, Chalmers Institute of Technology, 2004.

[30] Shadi A Dayeh, David PR Aplin, Xiaotian Zhou, Paul KL Yu, Edward T Yu, and Deli Wang. High electron mobility inas nanowire field-effect transistors. *Small*, 3(2):326–332, 2007.

[31] Seth A Fortuna and Xiuling Li. Metal-catalyzed semiconductor nanowires: a review on the control of growth directions. *Semiconductor Science and Technology*, 25(2):024005, 2010.

[32] Philippe Caroff, Kimberly A Dick, Jonas Johansson, ME Messing, Knut Deppert, and Lars Samuelson. Controlled polytypic and twin-plane superlattices in iii–v nanowires. *Nature Nanotechnology*, 4(1):50–55, 2009.

[33] Christophe Wilhelm, Alexandre Larrue, Xing Dai, Dmitri Migas, and Cesare Soci. Anisotropic photonic properties of iii–v nanowires in the zinc-blende and wurtzite phase. *Nanoscale*, 4(5):1446–1454, 2012.

[34] M Galicka, M Bukała, R Buczko, and P Kacman. Modelling the structure of gaas and inas nanowires. *Journal of Physics: Condensed Matter*, 20(45):454226, 2008.

[35] G Koblmüller, S Hertenberger, K Vizbaras, M Bichler, F Bao, JP Zhang, and G Abstreiter. Self-induced growth of vertical free-standing inas nanowires on si (111) by molecular beam epitaxy. *Nanotechnology*, 21(36):365602, 2010.

[36] I Zardo, S Conesa-Boj, F Peiro, JR Morante, J Arbiol, E Uccelli, G Abstreiter, and A Fontcuberta i Morral. Raman spectroscopy of wurtzite and zinc-blende gaas nanowires: polarization dependence, selection rules, and strain effects. *Physical Review B*, 80(24):245324, 2009.

[37] Anton Davydok. *X-ray diffraction analysis of InAs nanowires.* Dissertation Thesis, University of Siegen, 2013.

[38] Marion JL Sourribes, Ivan Isakov, Marina Panfilova, Huiyun Liu, and Paul A Warburton. Mobility enhancement by sb-mediated minimisation of stacking fault density in inas nanowires grown on silicon. *Nano letters*, 14(3):1643–1650, 2014.

[39] Andreas Biermanns, Steffen Breuer, Anton Davydok, Lutz Geelhaar, and Ullrich Pietsch. Structural evolution of self-assisted gaas nanowires grown on si (111). *Physica Status Solidi (RRL)-Rapid Research Letters*, 5(4):156–158, 2011.

[40] Jonas Johansson, KA Dick, Philippe Caroff, ME Messing, Jessica Bolinsson, Knut Deppert, and Lars Samuelson. Diameter dependence of the wurtzite-zinc blende transition in inas nanowires. *The Journal of Physical Chemistry C*, 114(9):3837–3842, 2010.

[41] Shadi A Dayeh, Darija Susac, Karen L Kavanagh, Edward T Yu, and Deli Wang. Structural and room-temperature transport properties of zinc blende

and wurtzite inas nanowires. *Advanced Functional Materials*, 19(13):2102–2108, 2009.

[42] Bernhard Mandl, Julian Stangl, Thomas Mårtensson, Anders Mikkelsen, Jessica Eriksson, Lisa S Karlsson, Günther Bauer, Lars Samuelson, and Werner Seifert. Au-free epitaxial growth of inas nanowires. *Nano letters*, 6(8):1817–1821, 2006.

[43] Kiyoshi Takahashi and Toyosaka Morizumi. Growth of inas whiskers in wurtzite structure. *Japanese Journal of Applied Physics*, 5(8):657, 1966.

[44] Christian Panse, Dominik Kriegner, and Friedhelm Bechstedt. Polytypism of gaas, inp, inas, and insb: an ab initio study. *Physical Review B*, 84(7):075217, 2011.

[45] Luis CO Dacal and A Cantarero. Ab initio calculations of indium arsenide in the wurtzite phase: structural, electronic and optical properties. *Materials Research Express*, 1(1):015702, 2014.

A

Appendix A : Bragg angles

Below are the usual planes conducted in XRD experiments and the related tilt (ω_{offset}) for common substrates.

Table A.1: Bragg and tilt angles of common substrates

Substrate	Lattice parameter(nm)	(hkl)	2θ of Bragg peak	Tilt
Si[001]	0.543102	004	69.1289	0
		224	88.0286	35.2644
		115	94.9508	15.7932
		044	106.7063	45
Si[111]	0.3828	111	28.41807	0
		224	88.02591	-19.4712
		333	94.93631	0
		115	94.9508	38.9425
GaAs[001]	0.5652	004	66.0700	0
		224	83.7752	35.2644
		115	90.1728	15.7932
		335	126.6837	40.3155
Ge[001]	0.565785	004	65.9930	0
		224	83.6690	35.6690
		044	100.7371	45
		115	90.0541	15.7932

Substrate	Lattice parameter(nm)	(hkl)	2θ of Bragg peak	Tilt
InP[001]	0.586875	004	63.3388	0
		224	80.0336	35.2644
		115	86.003	15.7932
		444	130.8332	54.7356
MgO[001]	0.4217	113	74.5774	25.2394
		004	93.8836	0
		133	105.5411	46.5085
		224	126.9842	35.2644
		115	143.3018	15.7932
$SrTiO_3$[001]	0.3905	003	72.5667	0
		113	81.7235	25.2394
		004	104.1915	0
		114	113.6288	19.4712

B

Appendix B : Out of Plane Sample Alignment

Before every measurement, to get a high intensity of the peaks, we do alignment procedures, also called as tilting axis adjustment. General ways for out of plane sample alignment is as follows

1. Connect the instrument with the software.
2. Set everything to 0.
3. Click on ”incident beam optics”. Make sure the beam attenuator is activated. I prefer to use pre-set intensity with activate level on 500.000 cps.
4. Do 2θ scan with 2θ range of 2 degrees and step size 0.01 degrees. This is to make sure that the source and detector is aligned. Take the highest peak (click right on the graph and choose ”peak mode” then ”move to” is more preferred) and change 2θ offset into the new 2θ value by clicking on ”user settings”, choose ”fine calibration offset” then choose ”set new = 0”. By doing this
5. To make sure that the beam is onto the sample, set z=8.5 then do z scan. Take the middle value of the sharply decreased signal using ”move mode”.
6. Make sure that we use the appropriate voltage and current of 45 kV and 40 mA to get the best intensity and resolution.
7. Choose unit cell of substrate and the hkl plane you want to measure. The software will give us the estimated value of ω and 2θ from its database. The corresponding ω_{offset} for different substrate and for different hkl is listed in Appendix 1.

8. Do a wide and rough omega scan with range 5 degrees and step size 0.03 degrees (preference). Take the highest peak, and then do a higher resolution omega scan with range 0.3 degrees and step size 0.001 degrees.

9. To further align the sample in order to gain higher intensity, do z, chi(especially for symmetric scan), and phi scan (especially for asymmetric scan). Z, chi, and phi scan can be done repeatedly until the values don't change much.

10. Once we get the best intensity from substrate, do a wide omega-2theta or 2theta-omega scan to get peaks from the thin film.

B.1 Reciprocal Space Mapping Procedure

For Reciprocal Space Mapping (RSM) scan procedure, we can further do it after we get the out of plane measurement results.

1. To do RSM scan, do out of plane ω-2θ or 2θ-ω scan to get range estimation on both ω and 2θ.

2. To begin, click on "file", choose "new program" and choose "2-axes measurement". Fill in the range and step size for both ω and 2θ based on the estimation we get from out of plane results. We can see the estimation time it will be done from the total time listed.

3. Click on "file", choose "new program", choose "General Batch" and the appropriate configuration.

4. Click on "insert batch settings" fill in the necessary parameters. For ω and 2θ, fill in the middle point values of the desired ranges.

5. Save the program then go to "measure" and choose "program".

6. Do not forget to appoint a folder to save the results before starting the measurement.

C

Appendix C : Time Comparison

Table C.1: Measurement time comparison table for each configuration and scan type

Configuration	scan type	sample	range(^{o})	step size(^{o})	time(hh:mm:ss)
HRXRD	$\omega - 2\theta$	A	10.7-17.7	0.01	00:02:43
		B	8-20	0.001	00:07:15
		C	11-17	0.01	00:02:08
X-Ray lens	$\omega - 2\theta$	A	8-28	0.01	00:06:41
		B	8-28	0.01	00:06:41
		C	8-28	0.01	00:06:41
HRXRD	RSM	A	$2\theta :$ 65-80	0.04	02:41:42
			$\omega :$ 10-21	0.04	
		B	$2\theta :$ 65-81	0.04	03:07:46
			$\omega :$ 10-21	0.04	
		C	$2\theta :$ 65-80	0.04	02:45:50
			$\omega :$ 10-21	0.04	
X-ray lens	RSM	A	$2\theta :$ 57-91	0.08	05:40:03
			$\omega :$ 9-26	0.08	
		B	$2\theta :$ 56-92	0.08	07:14:21
			$\omega :$ 8.5-26.5	0.08	
		C	$2\theta :$ 57-91	0.08	06:26:43
			$\omega :$ 10-26	0.08	
X-Ray lens	in plane ($2\theta - \omega$)	B	32.7-52.7	0.02	00:01:36